UNIVERSIDADE FEDERAL DE PERNAMBUCO
DEPARTAMENTO DE FÍSICA – CCEN
PROGRAMA DE PÓS-GRADUAÇÃO EM FÍSICA

PEDRO HENRIQUE DA SILVA SANTOS FERREIRA

FOUR-WAVE MIXING WITH HERMITE-GAUSS MODES IN RUBIDIUM VAPOR

Recife

2023

PEDRO HENRIQUE DA SILVA SANTOS FERREIRA

FOUR-WAVE MIXING WITH HERMITE-GAUSS MODES IN RUBIDIUM VAPOR

Dissertação apresentada ao Programa de Pós-graduação em Física da Universidade Federal de Pernambuco, como requisito parcial para a obtenção do título de Mestre em Física.

Área de Concentração: Óptica

Orientadora: Profa. Dra. Sandra Sampaio Vianna

Recife

2023

Catalogação na fonte
Bibliotecária Nataly Soares Leite Moro, CRB4-1722

F383f Ferreira, Pedro Henrique da Silva Santos
Four-wave mixing with hermite-gauss modes in rubidium vapor / Pedro Henrique da Silva Santos Ferreira. – 2023.
59 f.: il., fig.

Orientadora: Sandra Sampaio Vianna.
Dissertação (Mestrado) – Universidade Federal de Pernambuco. CCEN, Física, Recife, 2023.
Inclui referências.

1. Óptica. 2. Óptica não-linear. 3. Mistura de quatro ondas. 4. Perfil espacial. 5. Modos Hermite-Gauss. 6. Fase de Gouy. I. Vianna, Sandra Sampaio (orientadora). II. Título.

535.2 CDD (23. ed.) UFPE- CCEN 2023 - 136

PEDRO HENRIQUE DA SILVA SANTOS FERREIRA

FOUR-WAVE MIXING WITH HERMITE-GAUSS MODES IN RUBIDIUM VAPOR

Dissertação apresentada ao Programa de Pós-Graduação em Física da Universidade Federal de Pernambuco, como requisito parcial para a obtenção do título de Mestre em Física.

Aprovada em: 27/07/2023.

BANCA EXAMINADORA

_____

Profa. Dra. Sandra Sampaio Vianna
Orientadora
Universidade Federal de Pernambuco

_____

Prof. Dr. João Carlos de Aquino Carvalho
Examinador Interno
Universidade Federal de Pernambuco

_____

Prof. Dr. Eduardo Jorge da Silva Fonseca
Examinador Externo
Universidade Federal de Alagoas

AGRADECIMENTOS

Primeiramente, ao meu pai Jair, pelo amor e suporte incondicionais, por sempre me incentivar e fornecer as condições necessárias para os meus estudos. A trilha que percorri se tornou possível, em grande parte, graças ao seu apoio, e é a ele que dedico este trabalho.

À professora Sandra Vianna, pela disposição e mentoria ao longo dos anos. Sou grato pela sua dedicação admirável na minha jornada desde a graduação, quando fui seu aluno de iniciação científica.

À minha família, irmão, tios e primos, que sempre valorizaram os estudos e me incentivam incessamentemente, em especial a Jaira, Joana Dar'c, Luiza e Rubens (descanse em paz), que me inspiram verdadeiramente.

À Ma Nascimento, com quem divido os momentos de alegria, tristeza, euforia e melancolia, sejam eles relacionados a pós-graduação ou não. Muito obrigado pela sua amizade de uma década.

A Anderson Melo, que recentemente entrou em minha vida e já se tornou um dos meus maiores motivadores, agradeço por me encorajar, incentivar e por ser uma pessoa incrível.

Aos meus amigos Kel, Nath, Tayná e Ruan, agradeço pelo companheirismo, pelos momentos de descontração e pela consideração.

Aos professores do ensino básico que me inspiraram desde muito cedo a seguir esse caminho, em especial a Carlos, Marcos, Pedro e Lula (descanse em paz).

Aos professores do Departamento de Física que fizeram parte da minha formação.

Aos amigos do departamento: a Gabriel Fernandes, que conheci ainda em 2015 no curso de Engenharia, e tive a satisfação de me acompanhar até a presente etapa; aos colegas de laboratório Mateus, Raissa, Patrick e Alexandre, agradeço pelas discussões e pelo auxílio nos experimentos; aos colegas da graduação Habakuk e Alex, com quem tive diversas discussões ao longo das disciplinas; e aos colegas do grupo de Óptica, agradeço pelas discussões e pela descontração durante a hora do café. Sou grato pela amizade de todos vocês.

Por fim, agradeço à FACEPE, à CAPES e ao CNPq pelo apoio financeiro.

ABSTRACT

In this work, we present an experimental study on the spatial profile of coherent light generated in a forward four-wave mixing (FWM) process. We are interested in investigating how the transverse structure of the incident beams, more specifically of the Hermite-Gauss (HG) modes, is transferred to the generated signal in this nonlinear process. For the experiment, we used a continuous wave diode laser to excite a sample of Rubidium atoms, on the $^{85}\mathrm{Rb}$ D2 line, tuned to the frequency of the $5^2S_{1/2}\ (F = 3) \rightarrow 5^2P_{3/2}$ transition. With a Spatial Light Modulator, we were able to split the laser beam in two and structure them in the desired modes. These two beams, A and B, with wave vectors $\vec{k}_A$ and $\vec{k}_B$, and linear orthogonal polarizations, with quasi-copropagated configuration, were used to induce two FWM signals in the directions $2\vec{k}_A - \vec{k}_B$ and $2\vec{k}_B - \vec{k}_A$. The spatial profile of incident beams and the two nonlinear signals were captured by a CMOS camera, and the regimes of a thin or extensive medium were investigated. We were able to obtain results for a combination of gaussian-HG beams, as well as HG-HG beams. The profiles obtained by computer simulation were compared with the experimental measurements. Our theoretical model relies on solving the paraxial equation of the generated field. It leads to the overlap integrals of the incident beams, which unfold into some interesting selection rules in the transversal plane, for the thin and extensive medium regimes, and in the longitudinal axis, only for the long medium regime. Although the extensive medium regime presents some additional selection rules, the experimental requirements are difficult to achieve in our system, among them, we highlight the Gouy phase matching. On the other hand, a good agreement between theory and experiment was observed in the thin medium regime.

Keywords: Nonlinear optics. Four-wave mixing. Spatial profile. Hermite-Gauss modes. Gouy phase.

RESUMO

Neste trabalho, apresentamos um estudo experimental sobre o perfil espacial da luz coerente gerada num processo de mistura de quatro ondas (MQO) para frente. Estamos interessados em investigar como a estrutura transversal dos feixes, mais especificamente de modos Hermite-Gauss (HG), é transferida para os feixes gerados neste processo não-linear. No experimento, utilizamos um laser de diodo, contínuo, para excitar uma amostra de átomos de Rubídio, na linha D2 do $^{85}\mathrm{Rb}$, sintonizado na frequência da transição $5^2S_{1/2}\ (F=3) \rightarrow 5^2P_{3/2}$. Com um Modulador Espacial de Luz, foi possível dividir o feixe em dois e estruturá-los com os modos desejados. Esses dois feixes, A e B, com vetores de onda $\vec{k}_A$ e $\vec{k}_B$, e polarizações lineares e ortogonais, numa configuração quase-copropagante, foram utilizados para induzir dois sinais de MQO nas direções $2\vec{k}_A - \vec{k}_B$ e $2\vec{k}_B - \vec{k}_A$. Os perfis espaciais dos feixes incidentes e dos dois sinais não-lineares foram capturados com uma câmera CMOS e os regimes de meio fino e extenso foram investigados. Obtivemos resultados para uma combinação de feixes gaussiano-HG, assim como de feixes HG-HG. Os perfis obtidos por simulação em computador foram comparados com os resultados experimentais. Nosso modelo teórico consiste na solução da equação paraxial do feixe gerado. Ela leva às integrais de overlap dos feixes incidentes, que se desdobram em algumas regras de seleção interessantes no plano transversal, para os regimes de meio fino e extenso, e no eixo longitudinal, apenas para o regime de meio extenso. Embora o regime meio extenso apresente algumas regras de seleção adicionais, os requisitos experimentais são de difícil realização em nosso sistema, dentre eles, destacamos o casamento da fase de Gouy. Por outro lado, observamos um bom acordo entre a teoria e o experimento no regime de meio fino.

Palavras-chaves: Óptica não-linear. Mistura de quatro ondas. Perfil espacial. Modos Hermite-Gauss. Fase de Gouy.

LIST OF FIGURES

Figure 1 – Energy diagram for a two-level system. 13

Figure 2 – Dependence of the (a) population difference, and (b) real and (c) imaginary parts of the coherence on the detuning from resonance, for different amplitudes of the field $\Omega_{12} = \Omega$. 17

Figure 3 – Dependence of the (a) real and (b) imaginary parts of susceptibility on the detuning from resonance, for different amplitudes of the field $\Omega_{12} = \Omega$. . . . 18

Figure 4 – Comparison between normalized Doppler free and Doppler broadened profiles of (a) real and (b) imaginary parts of susceptibility, at room temperature ($T = 300\ \mathrm{K}$), for a field amplitude of $\Omega_{12} = \Gamma$, and $\Gamma = 2\pi \cdot 6.07\ \mathrm{MHz}$, which corresponds to the D2 line of ^{85}Rb. 20

Figure 5 – (a) Longitudinal profile of a Gaussian beam, with a visual demonstration of the beam parameters. (b) Transverse profile of a Gaussian beam. 23

Figure 6 – Transverse intensity and phase distribution of the first Hermite-Gaussian modes. 24

Figure 7 – General four-wave mixing scheme. (a) Shows three incident beams interacting with a nonlinear medium characterized by $\chi^{(3)}$, resulting in the generation of a nonlinear signal, (b) displays a possible energy diagram for this process, and (c) illustrates the orientation of the wavevectors in the process and the spatial phase mismatch $\Delta\vec{k} = \vec{k}_1 + \vec{k}_2 - \vec{k}_3 - \vec{k}_4$. 25

Figure 8 – (a) Shows the four-wave mixing setup in our experiment and (b) shows the wavevectors arrangement in the process, together with the phase mismatch. 27

Figure 9 – Rubidium 85 D2 transition hyperfine structure, with frequency splittings between the hyperfine energy levels. 28

Figure 10 – Right triangle with angle $\varphi = \tan^{-1}(z/z_R)$. 33

Figure 11 – Experimental setup. 35

Figure 12 – Comparison between the beam profile (a) before and (b) after the optical fiber. 36

Figure 13 – Saturated absorption spectroscopy setup. 37

Figure 14 – (a) Energy levels of a three-level system illustrating the crossover frequency. (b) The spectrum of the probe beam will exhibit an intermediate peak between the resonant frequencies. 38
Figure 15 – Saturated absorption spectrum of Rubidium in our system. The inset graph is a zoom of the $^{85}\mathrm{Rb}$ $(F_g = 3)$ Doppler curve. 38
Figure 16 – (a) LCOS-SLM inner structure and peripheral devices. (b) Representation of a liquid crystal molecule, highlighting its refractive indexes in each axis. . 39
Figure 17 – Composition of the mask to generate a HG_{01} mode. 40
Figure 18 – Amplitude modulation encoding onto the HG_{01} mask. 40
Figure 19 – (a) Example of masks used in our system and (b) their resulting beams. . . 41
Figure 20 – CMOS camera, model DCC1545M. 41
Figure 21 – Example of measurement and cleaning of the image. In (a) is the chosen frame of the observed nonlinear signal with scattered light, (b) and (c) are the chosen frames of the scattered light from beams A and B, respectively, and (d) is the result of the subtraction of the scattered light from the nonlinear signal. 43
Figure 22 – Comparison between (a) the grayscale gradient and (b) the color gradient applied to the signal presented in Figure 21(d). 43
Figure 23 – Illustration of the averaging method. The image represents a 20 x 20 image that will be averaged with a parameter $\ell = 4$. The red square represents the central pixel of the cluster, highlighted as the surrounding yellow squares. 44
Figure 24 – Comparison between the smoothing of the signal image for different values of the parameter ℓ. 45
Figure 25 – (a) Scheme of the beams crossing each other inside the cell. (b) Sketch of the guide masks used to align the beams. 46
Figure 26 – Intensity distribution of the incident beams used to perform the experiment in the gaussian-HG case, and their overlap in the position of the cell. . . . 47
Figure 27 – Intensity profile for a combination of gaussian-HG modes in the thin medium regime. Here, we show the intensity distribution of the incident u_A beams (u_B is gaussian in every case), and a comparison between the theoretical and experimental distribution of the nonlinear signals. 47

Figure 28 – Intensity profile for a combination of HG-HG modes, with $u_A = u_B$, in the thin medium regime. Here, we show the intensity distribution of the incident beams and a comparison between the theoretical and experimental distribution of the nonlinear signals. 48
Figure 29 – Intensity profile for a combination of HG-HG modes, with $u_A \neq u_B$, in the thin medium regime. Here, we show the intensity distribution of the incident beams and a comparison between the theoretical and experimental distribution of the nonlinear signals. 48
Figure 30 – Setups used to obtain the extensive regime. In the first setup (a) we focus both incident beams with a lens. In the second setup (b) we focus only beam A while keeping beam B wide. 49
Figure 31 – Input modes of the incident beams A and B. 50
Figure 32 – Transverse profiles and mode composition of the nonlinear signal $2A - B$ in the extensive and thin medium regimes, considering the incident beams from figure 31. 51
Figure 33 – Theoretical intensity profile for a combination of gaussian-HG modes in the extensive and thin medium regimes. Here, we show the intensity distribution of the incident u_A beam (u_B is gaussian in every case), the distribution of the theoretical nonlinear signal u_{2A-B} for each thickness regime, and diagrams representing the coefficients of the contributing modes to the nonlinear signals. 52
Figure 34 – Theoretical intensity profile for a combination of HG-HG modes, with $u_A = u_B$, in the extensive and thin medium regimes. Here, we show the intensity distribution of the incident beams, the distribution of the theoretical nonlinear signals for each thickness regime, and diagrams representing the coefficients of the contributing modes to the nonlinear signals. 52
Figure 35 – Theoretical intensity profile for a combination of HG-HG modes, with $u_A \neq u_B$, in the extensive and thin medium regimes. Here, we show the intensity distribution of the incident beams, the distribution of the theoretical nonlinear signals for each thickness regime, and diagrams representing the coefficients of the contributing modes to the nonlinear signals. 53

CONTENTS

1 INTRODUCTION 11

2 THEORETICAL FOUNDATION 13

2.1 LIGHT-MATTER INTERACTION 13

2.1.1 Bloch equations 15

2.1.2 Atomic susceptibility 18

2.1.3 Doppler broadening 19

2.2 PARAXIAL WAVE EQUATION AND HERMITE-GAUSS MODES 21

2.3 NONLINEAR OPTICS 24

2.3.1 Four-wave mixing 25

3 THEORETICAL MODEL 27

3.1 EXPERIMENTAL CONSIDERATIONS 27

3.2 SOLUTIONS TO THE PARAXIAL WAVE EQUATION 29

3.3 OVERLAP INTEGRALS 31

3.3.1 Transverse integrals 32

3.3.2 Longitudinal integrals 33

4 THE EXPERIMENT 35

4.1 EXPERIMENTAL SETUP 35

4.1.1 Saturated absorption spectroscopy setup 36

4.2 SPATIAL LIGHT MODULATOR 39

4.2.1 Generation of higher-order modes 40

4.3 MEASUREMENTS 41

5 RESULTS 46

5.1 THIN MEDIUM REGIME 46

5.2 EXTENSIVE MEDIUM REGIME 49

6 CONCLUSIONS 54

REFERENCES 56

1 INTRODUCTION

Nonlinear optics is a field of study that explores the optical phenomena that arise when the response of a material to an intense electromagnetic field is not linearly proportional to the field itself, but rather to higher powers of the field or to a combination of fields if more than one is applied [1]. It encompasses a wide range of phenomena and offers significant scientific and technological applications. This branch of optics has made significant progress in understanding and manipulating light-matter interactions, leading to breakthroughs in areas such as biophotonics [2], telecommunications [3], and quantum optics [4].

The historical roots of nonlinear optics can be traced back to preliminary papers published in the mid-20th century. A work published in 1941 [5] laid the foundations by investigating the optical properties of materials under intense electromagnetic fields even before the invention of lasers, which occurred in 1960, through the efforts of Theodore Maiman [6]. After the development of the laser, new concepts could finally be experimentally tested, such as optical harmonic generation [7], two-photon excitation [8], parametric amplification [9] and phase matching [10].

Concerning the phenomenon we're interested in, four-wave mixing is a third-order nonlinear effect that involves the interaction of multiple input electromagnetic waves to generate new waves at different frequencies, consisting of a combination (sum and/or difference) of the input frequencies. It was first described in the early 1960s [11], and in its initial years of study, most experiments were carried out using crystals as the nonlinear medium [12]. Nowadays it is broadly explored in various nonlinear media, such as semiconductor materials, optical fibers, gases, and various atomic vapors, which is the case we'll be focusing on in this work.

Structured light refers to light beams that have specific spatial intensity, phase patterns, and polarization state, deviating from the conventional Gaussian beam profiles. These patterns can take different forms. In this work, we explore Hermite-Gauss (HG) beam profiles, that are known to have a rectangular grating shape. They are solutions to the paraxial equation in a cartesian system of coordinates and have well-defined parity in each of the transversal axes [13]. Other examples of structured light are Laguerre-Gauss (LG) and Ince-Gauss (IG) beams. LG beams are solutions to the paraxial equation in a cylindrical system of coordinates, they have an optical vortex in their center, giving them a doughnut shape, and presenting a helical wavefront. These beams are known to carry orbital angular momentum as they propagate

[14]. IG beams are solutions to the paraxial equation in an elliptical system of coordinates and can be described as an intermediate case between Hermite and Laguerre beams. They are characterized by an eccentricity parameter that, when varied from zero to infinity, makes them closer to an HG or LG mode [15]. The paraxial equation will be derived in section 2.2. Structured light has gained significant attention in various fields of research, such as optical tweezers [16], communication [17], information [18], and astrophysics [19].

In recent years there has been some progress in the study of mode transfer in nonlinear mixing processes. Pires et al. studied in detail the occurrence of mode conversion in a two-wave mixing process using a variety of mode families, such as HG beams [20], whole and fractional orbital angular momentum LG beams [21, 22] and IG beams [23]. In another work, Rocha et al. [24] have made theoretical predictions on the generation of an almost pure HG mode as the result of four-wave mixing of two different HG modes. For this, they use a cascade three-level configuration in $^{85}\mathrm{Rb}$ vapor. Furthermore, the research conducted by Offer et al. [25] presented the importance of the Gouy phase effect in the different thickness regimes in four-wave mixing in atomic vapor. With their experiment, they demonstrated the generation of pure LG modes in the extensive medium regime.

In our research, we investigate a degenerate four-wave mixing in a heated rubidium vapor cell using Hermite-Gauss beams. Our objective is to study the transfer of transverse modes. In Chapter 2, we establish the foundations of our work, recapping the theory behind the mechanism of interaction between radiation and matter, leading to the optical Bloch equations. We also characterize Hermite-Gauss functions as solutions to the paraxial equation and describe a general four-wave mixing process as a nonlinear third-order process. In Chapter 3, we focused on the theoretical description of our system, deriving selection rules that govern the mode transfer, which we use to get computational results. In Chapter 4, we describe our experimental setup, measuring procedures, and data processing. In Chapter 5, we present our theoretical and experimental results making a comparison between them. In Chapter 6, we make conclusions about our work and present perspectives for future investigation.

2 THEORETICAL FOUNDATION

In this chapter, we present the fundamental concepts that support this research. We approach the problem of the interaction between radiation and matter, employing the density matrix formalism to describe the populations and coherences of a two-level atom, leading to the optical Bloch equations. We analyze the differential equations in the stationary regime, obtaining an expression for the population difference and coherence and relating it to the atomic susceptibility. Next, we characterize Hermite-Gauss beams as solutions to the paraxial equation. Finally, we discuss some basic concepts of nonlinear optics and introduce four-wave mixing source terms.

2.1 LIGHT-MATTER INTERACTION

To model the interaction between electromagnetic radiation and matter, we begin by considering a two-level atom, illustrated in figure 1, and taking electromagnetic radiation as a classical field, without quantizing it in terms of photons. We can describe this approach as semiclassical since it combines the classical nature of the electromagnetic field with the quantum structure of the atom's energy levels. This treatment is given in several textbooks, and we closely follow the approach taken by Yariv [26].

Figure 1 – Energy diagram for a two-level system.

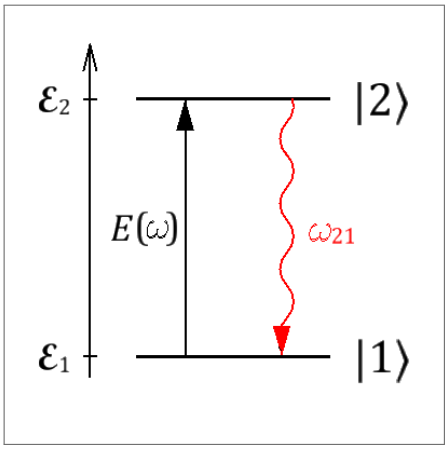

Source: the author (2023).

We start by considering the Hamiltonian of the system, which we separate in two terms, as

$$\widehat{\mathrm{H}} = \widehat{\mathrm{H}}_0 + \widehat{\mathrm{H}}_{int} \ . \tag{2.1}$$

The first term, $\widehat{\mathrm{H}}_0$, is the atom Hamiltonian, whose eigenstates are the states of the atom considered,

$$\widehat{\mathrm{H}}_0|j\rangle = \mathcal{E}_j|j\rangle, \qquad \text{for } j \in \{1,2\} \ , \tag{2.2}$$

where $\mathcal{E}_j$ is the energy of state $|j\rangle$. The second term, $\widehat{\mathrm{H}}_{int}$, is the interaction Hamiltonian, which we take as an electric dipole interaction, neglecting the magnetic component of the field, since its effect is much smaller in comparison. It can be written as

$$\widehat{\mathrm{H}}_{int} = -\vec{\mu}\cdot\vec{E}(\vec{r},t) \ , \tag{2.3}$$

where $\vec{\mu} = e\vec{r}$ is the atomic electric dipole operator. Its diagonal terms, $\vec{\mu}_{jj}$, are taken to be null, since dipole interactions connect states that are opposites in parity. We may write the dipole moment operator as

$$\vec{\mu} = \sum_{jk}\vec{\mu}_{jk}|j\rangle\langle k| \doteq \begin{pmatrix} 0 & \vec{\mu}_{12} \\ \vec{\mu}_{21} & 0 \end{pmatrix} \ . \tag{2.4}$$

$\vec{E}(\vec{r},t)$ is the electric field of the incident beam, which we can write as a monochromatic cosine wave of frequency ω and wave vector $\vec{k}$,

$$\begin{aligned} \vec{E}(\vec{r},t) &= \hat{\epsilon}\, E_0(\vec{r})\cos(\omega t) \ , \\ &= \hat{\epsilon}\,\frac{E_0(\vec{r})}{2}[e^{i\omega t} + e^{-i\omega t}] \ , \end{aligned} \tag{2.5}$$

where $\hat{\epsilon}$ is the polarization direction and $E_0(\vec{r})$ is a slow varying spatial profile, compared to the dimensions of the atoms. This way, we can write the components of the interaction Hamiltonian as

$$\begin{aligned} \widehat{\mathrm{H}}_{int,\,jk} &= \langle j|\widehat{\mathrm{H}}_{int}|k\rangle \ , \\ &= -\frac{\widetilde{\mu}_{jk}\, E_0(\vec{r})}{2}[e^{i\omega t} + e^{-i\omega t}] \ , \end{aligned} \tag{2.6}$$

where $\tilde{\mu}_{jk} = \vec{\mu}_{jk}\cdot\hat{\epsilon}$ is the projection of the dipole moment onto the electric field. Now, we define the Rabi frequency as

$$\Omega_{jk} = \frac{\widetilde{\mu}_{jk}\, E_0(\vec{r})}{2\hbar} \ , \tag{2.7}$$

and rewrite equation (2.6),

$$\widehat{\mathrm{H}}_{int,\,jk} = -\hbar\Omega_{jk}[e^{i\omega t} + e^{-i\omega t}] \ . \tag{2.8}$$

Next, we build the density matrix of the system. Density matrix formalism is useful when dealing with ensemble problems, in which the system is described by a statistical mixture

of individual samples [27]. Let's start by writing an arbitrary state of the atom as a linear combination of its eigenstates,

$$|\psi\rangle = \sum_j c_j |j\rangle \ , \tag{2.9}$$

and we define the density matrix in terms of the state of the system as

$$\hat{\rho} = |\psi\rangle\langle\psi| \ , \tag{2.10}$$

which gives

$$\hat{\rho} = \sum_{jk} \rho_{jk} |j\rangle\langle k| \doteq \begin{pmatrix} \rho_{11} & \rho_{12} \\ \rho_{21} & \rho_{22} \end{pmatrix} \ , \tag{2.11}$$

where the coefficients of $\hat{\rho}$ are given in terms of the coefficients of the wave function as

$$\rho_{jk} = c_j c_k^* \ . \tag{2.12}$$

The diagonal terms of the density matrix, ρ_{jj}, are called population terms and represent the percentage of atoms in the ensemble that are in the state $|j\rangle$. On the other hand, the off-diagonal terms, ρ_{jk}, for $j \neq k$, are called coherence terms, and represent how well coupled are the levels considered. These are directly related to the response of the medium in which the field is being applied. The normalization condition of the wave function leads to the normalization condition of the matrix trace,

$$\mathrm{Tr}(\hat{\rho}) = 1 \ , \tag{2.13}$$

which denotes probability conservation. It means that the probability associated with all possible outcomes is 1, i.e., we are sure to find an atom in any one of the energy states.

2.1.1 Bloch equations

The evolution of the density matrix is governed by Liouville's equation, given by

$$\frac{d\hat{\rho}}{dt} = \frac{i}{\hbar}[\hat{\rho}, \widehat{\mathrm{H}}] \ , \tag{2.14}$$

where the square brackets refer to the commutator of the operators. Direct substitution of $\hat{\rho}$ and $\widehat{\mathrm{H}}$ gives us the following equations:

$$\frac{d\rho_{11}}{dt} = \frac{i}{\hbar}(\rho_{12}\mathrm{H}_{21} - \rho_{21}\mathrm{H}_{12}) \ , \tag{2.15}$$

$$\frac{d\rho_{22}}{dt} = \frac{i}{\hbar}(\rho_{21}\mathrm{H}_{12} - \rho_{12}\mathrm{H}_{21}) \ , \tag{2.16}$$

$$\frac{d\rho_{12}}{dt} = \frac{i}{\hbar}[\rho_{12}(\mathcal{E}_1 - \mathcal{E}_2) + (\rho_{11} - \rho_{22})\mathrm{H}_{12}] \ , \tag{2.17}$$

$$\frac{d\rho_{21}}{dt} = \frac{i}{\hbar}[\rho_{21}(\mathcal{E}_2 - \mathcal{E}_1) + (\rho_{22} - \rho_{11})\mathrm{H}_{21}] \ , \tag{2.18}$$

which we can rewrite as

$$\frac{d}{dt}(\rho_{22} - \rho_{11}) = \frac{2i}{\hbar}(\rho_{12}\mathrm{H}_{21} - \rho_{21}\mathrm{H}_{12}) \ , \tag{2.19}$$

$$\frac{d\rho_{12}}{dt} = \frac{i}{\hbar}\left[\rho_{12}(\mathcal{E}_1 - \mathcal{E}_2) - (\rho_{22} - \rho_{11})\mathrm{H}_{12}\right] \ . \tag{2.20}$$

Up until now, we made no considerations concerning relaxation terms. Dissipation of energy should naturally arise from spontaneous decay, mostly due to collisions [26]. Assuming the relaxation follows an exponential law, we should add a decay term of Γ for the population terms and $\Gamma/2$ for the coherence terms [28],

$$\frac{d\Delta\rho_{21}}{dt} = \frac{2i}{\hbar}(\rho_{12}\mathrm{H}_{21} - \rho_{21}\mathrm{H}_{12}) - (\Delta\rho_{21} - \Delta\rho_{21}^0)\Gamma \ , \tag{2.21}$$

$$\frac{d\rho_{12}}{dt} = \frac{i}{\hbar}[\rho_{12}(\mathcal{E}_1 - \mathcal{E}_2) - (\rho_{22} - \rho_{11})\mathrm{H}_{12}] - \rho_{12}\frac{\Gamma}{2} \ . \tag{2.22}$$

$\Delta\rho_{21} = \rho_{22} - \rho_{11}$ is the difference between the populations, $\Delta\rho_{21}^0$ is the population difference in the absence of radiation, and it's easy to see that $\rho_{12} = \rho_{21}^*$. Equations (2.21) and (2.22) are the so-called *optical* Bloch equations. They describe the time evolution of a two-level atom excited by radiation close to the resonance of a transition, decaying by spontaneous emission. Now, we decompose the coherence in terms that vary fast and slowly,

$$\rho_{12} = \sigma_{12}e^{i\omega t} \ , \tag{2.23}$$

substituting it in the optical Bloch equations, along with H_{12} and H_{21}, and making the rotating wave approximation (RWA), we arrive at

$$\frac{d\Delta\rho_{21}}{dt} = 2i(\sigma_{12}\Omega_{21} - \sigma_{21}\Omega_{12}) - (\Delta\rho_{21} - \Delta\rho_{21}^0)\Gamma \ , \tag{2.24}$$

$$\frac{d\rho_{12}}{dt} = i\Omega_{12}\Delta\rho_{21} - \sigma_{12}(i\delta + \Gamma/2) \ , \tag{2.25}$$

where $\delta = \omega - \omega_0$ is the detuning of the laser to the resonance frequency of the system, defined as $\omega_0 = (E_2 - E_1)/\hbar$.

We expect that for long application time intervals of the field, the system should reach equilibrium, where the populations and coherences enter a steady state, which we call a stationary regime. To analyze the stationary solutions of the system, we should put

$$\frac{d\Delta\rho_{21}}{dt} = 0 \quad \text{and} \quad \frac{d\rho_{12}}{dt} = 0 \,, \tag{2.26}$$

leaving us with a system of equations:

$$2i(\sigma_{12}\Omega_{21} - \sigma_{21}\Omega_{12}) - (\Delta\rho_{21} - \Delta\rho_{21}^0)\Gamma = 0 \,, \tag{2.27}$$

$$i\Omega_{12}\Delta\rho_{21} - \sigma_{12}(i\delta + \Gamma/2) = 0 \,. \tag{2.28}$$

Solving for $\Delta\rho_{21}$ and σ_{12}, we get the solutions

$$\Delta\rho_{21} = \frac{\delta^2 + \Gamma^2/4}{2|\Omega_{12}|^2 + \delta^2 + \Gamma^2/4}\Delta\rho_{21}^0 \,, \tag{2.29}$$

$$\sigma_{12} = -\frac{\Omega_{12}(\delta + i\Gamma/2)}{2|\Omega_{12}|^2 + \delta^2 + \Gamma^2/4}\Delta\rho_{21}^0 \,. \tag{2.30}$$

Figure 2 – Dependence of the (a) population difference, and (b) real and (c) imaginary parts of the coherence on the detuning from resonance, for different amplitudes of the field $\Omega_{12} = \Omega$.

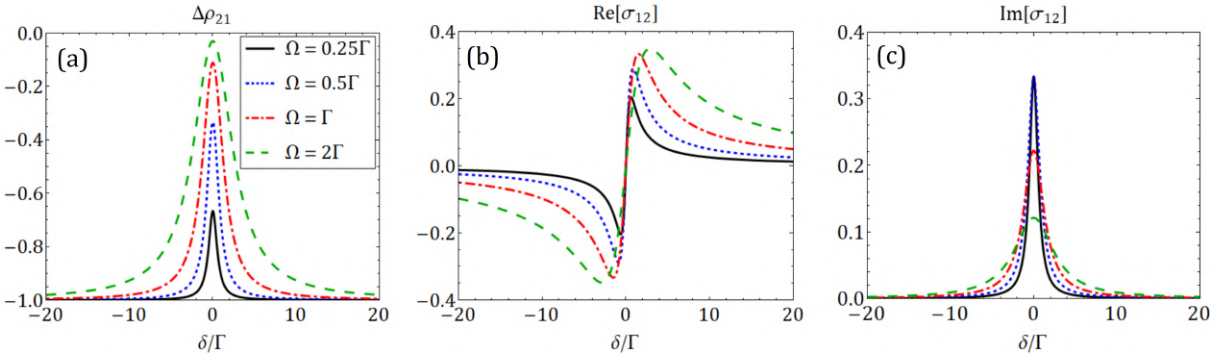

Source: the author (2023).

In Figure 2, we plot the quantities we derived in the stationary regime in terms of the detuning of the laser from resonance, considering that in the absence of radiation, the population is fully in the ground state, $\Delta\rho_{21}^0 = -1$. In (a), the population difference tends to zero for stronger fields near resonance. In (b) and (c), we notice that the real and imaginary parts of coherence have a behavior similar to that of refraction and absorption, respectively. This will become clear when we derive the atomic susceptibility next. In (c), we can also notice *power broadening*, i.e., the enlargement of the spectral line width due to saturation of the system under higher powers of the field.

2.1.2 Atomic susceptibility

To evaluate the response of the system, we express the macroscopic polarization induced by the field as

$$\vec{P} = N\langle\vec{\mu}\rangle = N\mathrm{Tr}(\hat{\rho}\vec{\mu}) \ , \tag{2.31}$$

where N is the atomic density. Expanding and projecting this expression onto the outer field, we get

$$\vec{P}\cdot\hat{\epsilon} = N\left(\tilde{\mu}_{21}\sigma_{12}e^{i\omega t} + \tilde{\mu}_{12}\sigma_{21}e^{-i\omega t}\right) . \tag{2.32}$$

Substitution of (2.30) into (2.32) gives

$$\vec{P}\cdot\hat{\epsilon} = \frac{N|\tilde{\mu}_{12}|^2E_0}{\hbar}\left[\frac{\delta\cos(\omega t) - (\Gamma/2)\sin(\omega t)}{2|\Omega_{12}|^2 + \delta^2 + \Gamma^2/4}\right]\Delta\rho_{21}^0 \ . \tag{2.33}$$

We can also express the polarization of the medium in terms of the atomic susceptibility, $\chi = \chi' - i\chi''$, as

$$\begin{aligned}\vec{P} &= \mathrm{Re}[\varepsilon_0\chi\vec{E}_0e^{i\omega t}] \ , \\ \vec{P}\cdot\hat{\epsilon} &= \varepsilon_0E_0[\chi'\cos(\omega t) + \chi''\sin(\omega t)] \ .\end{aligned} \tag{2.34}$$

Comparison between equations (2.33) and (2.34) results in

$$\chi' = \frac{N|\tilde{\mu}_{12}|^2\delta\Delta\rho_{21}^0}{\varepsilon_0\hbar(2|\Omega_{12}|^2 + \delta^2 + \Gamma^2/4)} \ , \tag{2.35}$$

$$\chi'' = -\frac{N|\tilde{\mu}_{12}|^2(\Gamma/2)\Delta\rho_{21}^0}{\varepsilon_0\hbar(2|\Omega_{12}|^2 + \delta^2 + \Gamma^2/4)} \ . \tag{2.36}$$

Figure 3 – Dependence of the (a) real and (b) imaginary parts of susceptibility on the detuning from resonance, for different amplitudes of the field $\Omega_{12} = \Omega$.

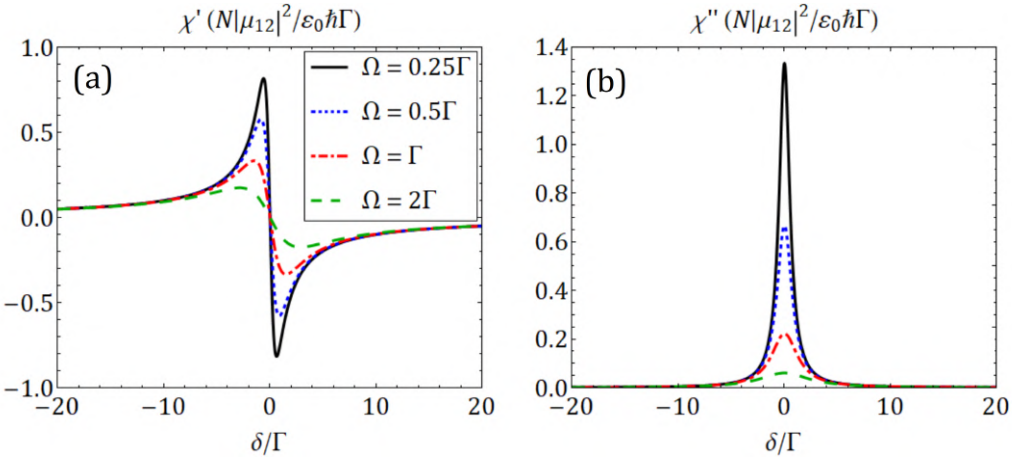

Source: the author (2023).

In Figure 3, we plot the susceptibility as a function of the detuning. Due to its direct derivation from the coherence, they present a similar behavior as shown in figure 2, aside from some scaling constants. The susceptibility is related to a complex refractive index [29] through the relation

$$\widetilde{n} = \sqrt{\varepsilon} = \sqrt{1+\chi}\,, \tag{2.37}$$

which, for $\chi \ll 1$, can be expanded as

$$\widetilde{n} \approx 1 + \frac{\chi}{2} + \mathcal{O}(\chi^2)\,. \tag{2.38}$$

We may define

$$\widetilde{n} = n + i\kappa\,, \tag{2.39}$$

where n is the usual refractive index, and κ is related to the absorption coefficient [30]. The comparison between equations (2.38) and (2.39) associates the susceptibility with the optical properties of the medium,

$$n = 1 + \chi'/2\,, \tag{2.40}$$

$$\kappa = -\chi''/2\,. \tag{2.41}$$

2.1.3 Doppler broadening

The motion of the atoms at room temperature induces the Doppler effect, which makes the atoms feel an incoming field with a shifted frequency,

$$\omega' = \omega - \vec{k}\cdot\vec{v}\,, \tag{2.42}$$

where $\vec{v}$ is the velocity of the atom. If the atom moves toward the beam, it experiences a blueshift, whereas if it moves away from the beam, it experiences a redshift. We might rewrite the detuning of the laser to take this shift into account,

$$\delta' = \delta - \vec{k}\cdot\vec{v}\,. \tag{2.43}$$

To account for the effect of this shift, we need to consider the distribution of velocities among the atoms in the sample. For simplicity, we are assuming the Maxwell-Boltzmann distribution of velocity in one dimension, which obeys a Gaussian distribution [31],

$$f(v) = \frac{1}{u\sqrt{\pi}}\exp\left(-\frac{v^2}{u^2}\right)\,, \tag{2.44}$$

where u is the most probable velocity of the atoms in the ensemble, given by

$$u = \sqrt{\frac{2k_B T}{m}} \,, \tag{2.45}$$

k_B is the Boltzmann constant, and T is the temperature of the system. This distribution will serve as a weight function to integrate the susceptibility over all velocities,

$$\begin{aligned} \chi(\delta) &= \int_{-\infty}^{\infty} f(v)\, \widetilde{\chi}(\delta')\, dv \,, \\ &= \int_{-\infty}^{\infty} f(v)\, \widetilde{\chi}(\delta - kv)\, dv \,. \end{aligned} \tag{2.46}$$

Figure 4 – Comparison between normalized Doppler free and Doppler broadened profiles of (a) real and (b) imaginary parts of susceptibility, at room temperature ($T = 300$ K), for a field amplitude of $\Omega_{12} = \Gamma$, and $\Gamma = 2\pi \cdot 6.07$ MHz, which corresponds to the D2 line of ^{85}Rb.

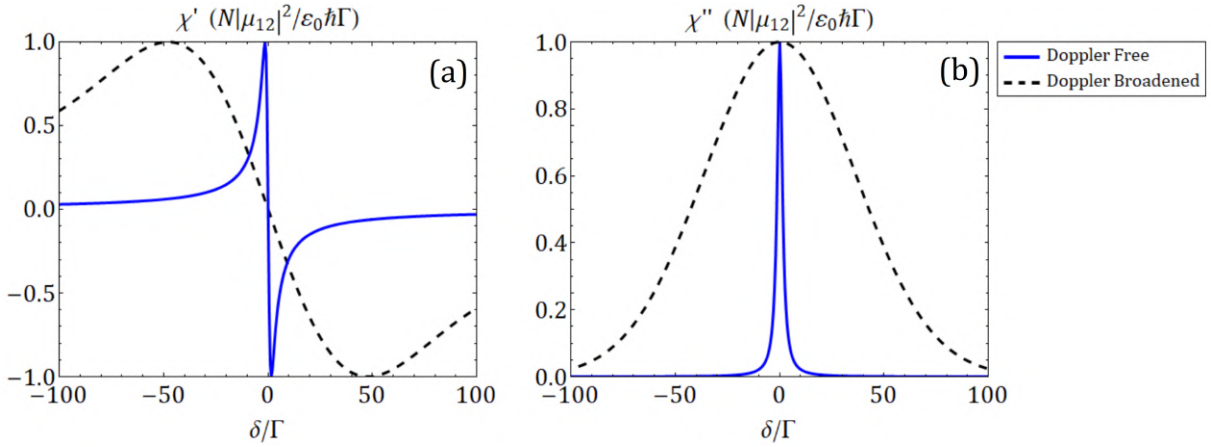

Source: the author (2023).

Figure 4 shows a comparison between the natural line and an enlarged Doppler line of susceptibilities under room temperature. The Doppler-free profile of the imaginary part has a Lorentzian shape, while the Doppler broadened line has what is called a *Voigt* shape, i.e., the convolution between a Lorentzian and a Gaussian curve. This difference in the width of the lines is exploited when performing saturated absorption spectroscopy, in which Doppler-free lines are carved over the Doppler broadened profiles (see subsection 4.1.1).

2.2 PARAXIAL WAVE EQUATION AND HERMITE-GAUSS MODES

Hermite-Gauss functions are a set of solutions to the homogeneous paraxial wave equation. To derive the paraxial wave equation we start by writing Maxwell's equations inside matter:

$$\nabla \cdot \vec{D} = \rho \,, \tag{2.47}$$

$$\nabla \cdot \vec{B} = 0 \,, \tag{2.48}$$

$$\nabla \times \vec{E} = -\frac{\partial \vec{B}}{\partial t} \,, \tag{2.49}$$

$$\nabla \times \vec{H} = \vec{J} + \frac{\partial \vec{D}}{\partial t} \,, \tag{2.50}$$

where $\vec{E}$ is the electric field, $\vec{B}$ is the magnetic flux density, $\vec{D} = \varepsilon_0 \vec{E} + \vec{P}$ is the electric displacement, $\vec{P}$ is the polarization, $\vec{H} = \vec{B}/\mu_0 - \vec{M}$ is the magnetic field, $\vec{M}$ is the magnetization and ρ and $\vec{J}$ are the distributions of free charge and current. Manipulation of these equations takes to the wave equation,

$$\nabla^2 \vec{E} - \frac{n^2}{c^2} \frac{\partial^2 \vec{E}}{\partial t^2} = \mu_0 \frac{\partial^2 \vec{P}}{\partial t^2} \,, \tag{2.51}$$

where n is the refractive index. This equation indicates that the polarization acts as a source for the electromagnetic field. Next, to get rid of the time dependence, we make the substitutions $\vec{E}(\vec{r}, t) = \hat{\epsilon} E(\vec{r}) e^{-i\omega t}$ and $\vec{P}(\vec{r}, t) = \hat{\epsilon} P(\vec{r}) e^{-i\omega t}$. This simplifies the equation to the so-called Helmholtz equation,

$$\nabla^2 E + k^2 E = -\frac{k^2}{\varepsilon_0} P \,. \tag{2.52}$$

Next, we make the paraxial approximation, which first consists in separating the fast oscillation component of the fields in the propagation direction, $E(\vec{r}) = u(\vec{r}) e^{ikz}$ and $P(\vec{r}) = p(\vec{r}) e^{ikz}$. Here we consider a wave propagating in the z direction, and $u(\vec{r})$ and $p(\vec{r})$ are smoothly varying envelopes, carrying information about the transverse shape of the beams. Making this substitution, the equation becomes

$$\nabla_\perp^2 u + \frac{\partial^2 u}{\partial z^2} + 2ik \frac{\partial u}{\partial z} = -\frac{k^2}{\varepsilon_0} p \,, \tag{2.53}$$

where $\nabla_\perp^2$ is the Laplacian operator in the transverse plane. The second part of the paraxial approximation is based on the assumption that the curvature of the envelope varies slowly,

$$\left| \frac{\partial^2 u}{\partial z^2} \right| \ll k \left| \frac{\partial u}{\partial z} \right| \ll k^2 \left| u \right| \,. \tag{2.54}$$

This condition is necessary to prevent the beam from rapidly diverging. We may write the inhomogeneous paraxial equation,

$$\nabla_{\perp}^{2} u + 2ik\frac{\partial u}{\partial z} = -\frac{k^2}{\varepsilon_0} p \,. \tag{2.55}$$

Homogeneous solutions are vacuum solutions, characterized by no source term. So for now, we should look for the case where $p = 0$,

$$\nabla_{\perp}^{2} u + 2ik\frac{\partial u}{\partial z} = 0 \,. \tag{2.56}$$

Several families of functions may arise as solutions to this equation depending on the system of coordinates considered. In this work, we are interested in Hermite-Gauss functions, which emerge as solutions in a Cartesian system of coordinates. Therefore, we should make the substitution

$$\frac{\partial^2 u}{\partial x^2} + \frac{\partial^2 u}{\partial y^2} + 2ik\frac{\partial u}{\partial z} = 0 \,. \tag{2.57}$$

First, let us express the Gaussian solution to introduce some parameters and properties common to all other solutions,

$$u_{\mathrm{G}}(x, y, z) = C\frac{w_0}{w(z)} \exp\left[-\frac{x^2 + y^2}{w^2(z)}\right] \exp\left[ik\frac{x^2 + y^2}{2R(z)}\right] \exp\left[-i\psi_{\mathrm{G}}(z)\right] , \tag{2.58}$$

where C is a normalization constant; $w(z) = w_0\sqrt{1 + (z/z_R)^2}$ is the waist parameter (radius of the transverse profile) and w_0 is the minimum waist; $R(z) = z\left[1 + (z_R/z)^2\right]$ is the radius of curvature of the wavefront; $z_R = \pi w_0^2/\lambda$ is the Rayleigh length, which characterizes the divergence of the beam, representing the distance over which the beam propagates from the focus point while its cross-sectional area doubles; and the term $\psi_{\mathrm{G}}(z) = \tan^{-1}(z/z_R)$ is the Gouy phase, which is a gradually acquired phase as the beam propagates. The beam accumulates a maximum phase of π as it propagates from $z = -\infty$ to $+\infty$. Figure 5 illustrates the longitudinal and transverse profiles of a Gaussian beam, highlighting its parameters listed above.

From the illustration, we can see that the beam diverges as it propagates, approaching the shape of a cone far from the minimum waist. The angle Θ inside that cone defines the divergence of the beam. It can be calculated by the expression

$$\Theta = 2\lim_{z\to\infty}\frac{dw(z)}{dz} \,, \tag{2.59}$$

which evaluates to

$$\Theta = \frac{2\lambda}{\pi w_0} \,. \tag{2.60}$$

Figure 5 – (a) Longitudinal profile of a Gaussian beam, with a visual demonstration of the beam parameters. (b) Transverse profile of a Gaussian beam.

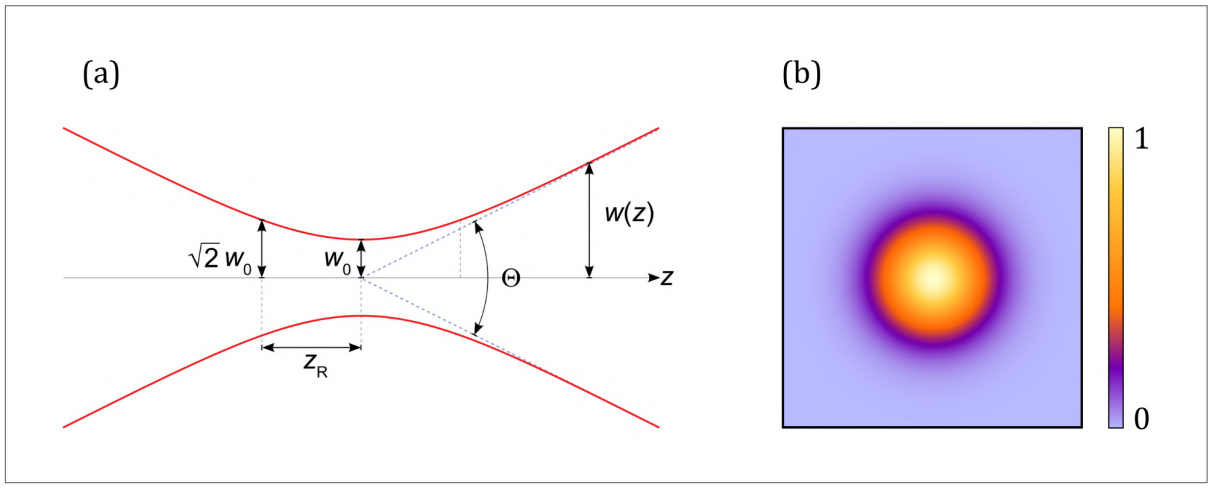

Source: (a) from reference [32] and (b) the author (2023).

The divergence is inversely proportional to the beam spot size. A Gaussian beam that is harshly focused to a small spot diverges quickly as it travels away from the focus. On the other hand, to reduce the divergence of a laser beam in the far field and maximize its peak intensity at greater distances, the beam must have a larger cross-section at the minimum waist. This relationship between the divergence of a beam and its width is fundamental to the theory of diffraction of light [33], and it does not depend on the intensity profile of the beam.

Finally, Hermite-Gauss functions are expressed as

$$\begin{aligned}\mathrm{HG}_{mn}(x,y,z) =& \sqrt{\frac{2}{\pi}}\frac{C_{mn}}{w(z)}\mathrm{H}_m\left(\frac{\sqrt{2}x}{w(z)}\right)\mathrm{H}_n\left(\frac{\sqrt{2}y}{w(z)}\right)\exp\left[-\frac{x^2+y^2}{w^2(z)}\right] \\ &\times \exp\left[ik\frac{x^2+y^2}{2R(z)}\right]\exp\left[-i\psi_{\mathrm{HG}}(z)\right].\end{aligned} \tag{2.61}$$

These solutions are characterized by two integer indices, m and n, with $m, n \geq 0$, each pair (m, n) defines a mode. $C_{mn} = \sqrt{2^{-(m+n)}/m!n!}$ are normalization constants for each mode and $\mathrm{H}_j(\xi)$ is a Hermite polynomial of order j in the variable ξ. The Gouy phase for a Hermite-Gauss mode is defined as $\psi_{\mathrm{HG}}(z) = (N+1)\tan^{-1}(z/z_R)$ and depends on the mode order of the beam, defined as $N = m+n$. It should be noted that the Gaussian beam is a particular case of the Hermite-Gaussian modes, for which $(m, n) = (0, 0)$. In this case, the Hermite polynomials are simple constants, and all other changes produced by m and n vanish. In contrast with the Gaussian case, higher-order Hermite-Gaussian modes accumulate a maximum phase of $(N+1)\pi$ as they propagate from $z = -\infty$ to $+\infty$. All the other parameters are defined just as was presented in the Gaussian case.

Hermite-Gauss functions constitute an orthogonal and complete set of solutions to the paraxial equation, expressed in the relations:

$$\iint \mathrm{HG}_{mn}(\vec{r})\,\mathrm{HG}^{*}_{m'n'}(\vec{r})\,dxdy = \delta_{m\,m'}\,\delta_{n\,n'}\,, \tag{2.62}$$

$$\sum_{m,n} \mathrm{HG}_{mn}(\vec{r})\,\mathrm{HG}^{*}_{mn}(\vec{r'}) = \delta(x-x',\,y-y')\,. \tag{2.63}$$

These properties imply that any solution to the equation can be expressed as a unique linear combination of HG modes. They also present a well-defined parity in each axis, equal to those of the associated Hermite polynomials. They have a rectangular grating-like shape and a phase distribution that resembles a chessboard. These spatial properties can be seen in Figure 6.

Figure 6 – Transverse intensity and phase distribution of the first Hermite-Gaussian modes.

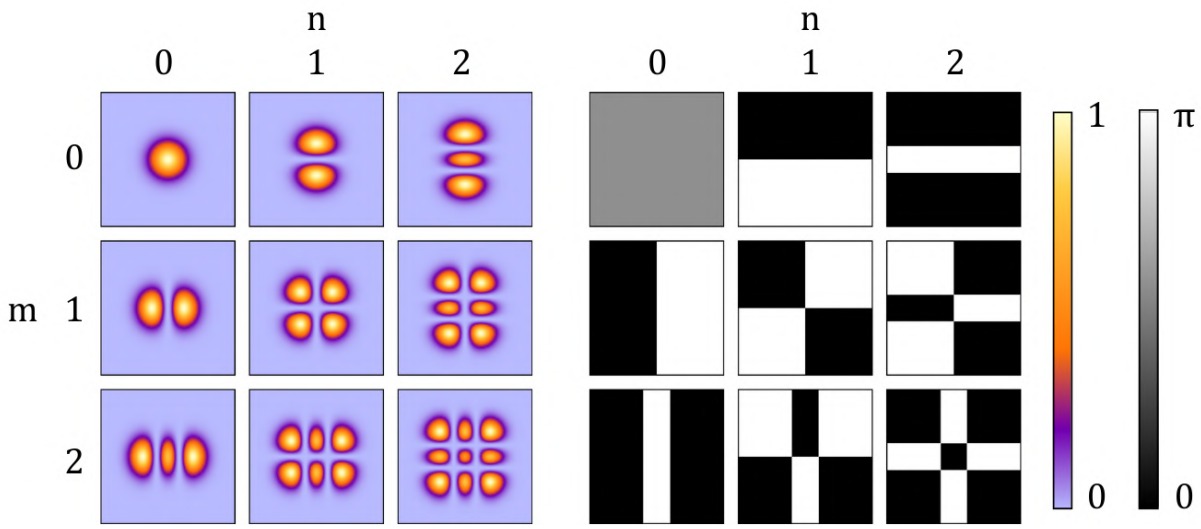

Source: the author (2023).

2.3 NONLINEAR OPTICS

Nonlinear optical phenomena usually arise from the application of an intense electromagnetic field to an optically nonlinear material. In the case of linear optics, we describe the response of the material as an induced polarization, which depends linearly on the electric field strength and is often written as the relation

$$\vec{P} = \varepsilon_0 \overleftrightarrow{\chi}^{(1)} \otimes \vec{E}\,. \tag{2.64}$$

The term $\overleftrightarrow{\chi}^{(1)}$ represents the linear susceptibility of the material. In the case of nonlinear optics, the material's response can be described by expressing the induced polarization as a

power series in the field strength, with each power corresponding to an order of the nonlinear polarization as

$$\begin{aligned}\vec{P} &= \vec{P}^{(1)} + \vec{P}^{(2)} + \vec{P}^{(3)} + \cdots \\ &= \varepsilon_0(\overleftrightarrow{\chi}^{(1)} \otimes \vec{E} + \overleftrightarrow{\chi}^{(2)} \otimes \vec{E}\vec{E} + \overleftrightarrow{\chi}^{(3)} \otimes \vec{E}\vec{E}\vec{E} + \cdots) \,,\end{aligned} \tag{2.65}$$

where $\vec{P}^{(n)} = \varepsilon_0 \overleftrightarrow{\chi}^{(n)} \otimes \vec{E}^n$ is the nonlinear polarization of order n. Each $\overleftrightarrow{\chi}^{(n)}$ is a tensor of order $n+1$, containing 3^{n+1} components. They represent nonlinear susceptibilities of order n and are responsible for several nonlinear optical phenomena. In general, symmetries of the problem should be considered to reduce the complexity of these terms. For instance, centrosymmetric media, such as atomic vapors, present null even order susceptibilities, $\overleftrightarrow{\chi}^{(2n)} = 0$.

The importance of polarization in the description of nonlinear optical phenomena arises from its ability to generate new spectral components of the electromagnetic field. This is evident from the wave equation inside matter (2.51).

2.3.1 Four-wave mixing

Four-wave mixing (FWM) is a third-order process in which the interaction between three fields in a nonlinear medium generates a fourth one. The frequency of the generated field must be a linear combination of the frequencies of the input fields. Figure 5 illustrates a general case of FWM, where the atomic system interacts with incident fields whose frequencies are ω_1, ω_2 and ω_3, and generates a new field with frequency ω_4. We consider, for example, that $\omega_4 = \omega_1 + \omega_2 - \omega_3$.

Figure 7 – General four-wave mixing scheme. (a) Shows three incident beams interacting with a nonlinear medium characterized by $\chi^{(3)}$, resulting in the generation of a nonlinear signal, (b) displays a possible energy diagram for this process, and (c) illustrates the orientation of the wavevectors in the process and the spatial phase mismatch $\Delta\vec{k} = \vec{k}_1 + \vec{k}_2 - \vec{k}_3 - \vec{k}_4$.

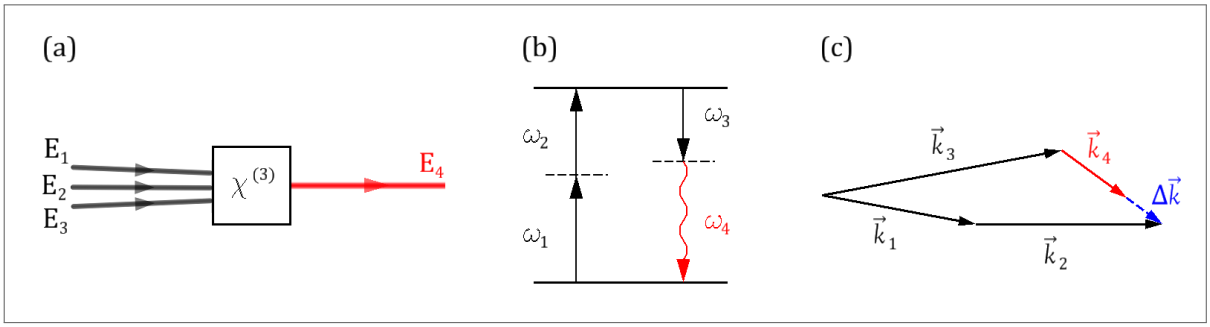

Source: the author (2023).

This example can be modeled by a field containing three spectral components with plane wavefronts,

$$E(t) = E_1 e^{-i\omega_1 t} + E_2 e^{-i\omega_2 t} + E_3 e^{-i\omega_3 t} + \text{c.c.} \,. \tag{2.66}$$

Calculation of the third-order polarization induced in the medium as $P = [E(t)]^3$ outputs 44 different frequency components if positive and negative frequencies are considered distinct. Usually, experimental setups are built to observe a specific component. If we write the induced polarization as

$$P(t) = \sum_n \tilde{p}_n(\omega_n) e^{-i\omega_n t} \,, \tag{2.67}$$

where $\tilde{p}_n(\omega_n)$ is the coefficient of each frequency component of the induced polarization. The component $\tilde{p}_4(\omega_4)$ in the example is

$$\tilde{p}_4(\omega_1 + \omega_2 - \omega_3) = 6\varepsilon_0 \chi^{(3)} E_1 E_2 E_3^* \,. \tag{2.68}$$

It is important to note that $\chi^{(3)}$ itself depends on the frequencies of the fields, or better said, on the coherences of the medium. Nonlinear optical processes involve the coupling of multiple photons, resulting in the generation of new frequencies. The strength of this coupling and the efficiency of the nonlinear process depend on the specific coherences present in the medium. Therefore, $\chi^{(3)}$ is larger and the nonlinear process occurs more efficiently when the frequencies involved are close to the resonant frequencies of the medium.

The spatial dependence of the fields gives rise to phase matching conditions, which are determined by the solution of the wave equation (2.51). These conditions play a crucial role in ensuring efficient signal generation. In particular, the intensity of the nonlinear signal follows a relation given by

$$I_4 \propto \text{sinc}^2(\Delta k L) \,, \tag{2.69}$$

where L represents the length of the medium. The behavior of the sinc function indicates that the signal strength is maximized when the phase mismatch (Δk) is minimized. Considering experimental conditions, this implies that the angle between the incident beams should be small.

3 THEORETICAL MODEL

In this chapter, we build the theoretical model that describes the mode transfer in the four-wave mixing process we worked on. We begin by describing the four-wave mixing setup we perform experimentally and translate it into a theoretical description. Next, we solve the paraxial wave equation considering a third-order nonlinear polarization. Selection rules arise from the solution of the wave equation, with particular considerations regarding the thickness of the medium. With these selection rules, we can obtain theoretical results for the expected intensity distribution, as well as the exact contribution of the modes participating in the nonlinear signal.

3.1 EXPERIMENTAL CONSIDERATIONS

We start this section by showing the four-wave mixing setup in our experimental system. We focus two incident beams in a vapor cell. They are denoted by E_A and E_B, have linear polarizations that are orthogonal to each other, and are aligned in a quasi-copropagated arrangement. On the other side of the cell, in addition to the transmitted beams, $\widetilde{E}_A$ and $\widetilde{E}_B$, the beams generated by the nonlinear process, E_{2A-B} and E_{2B-A}, emerge. The beams originate from the same laser source, resulting in coherence and phase synchronization.

Figure 8 – (a) Shows the four-wave mixing setup in our experiment and (b) shows the wavevectors arrangement in the process, together with the phase mismatch.

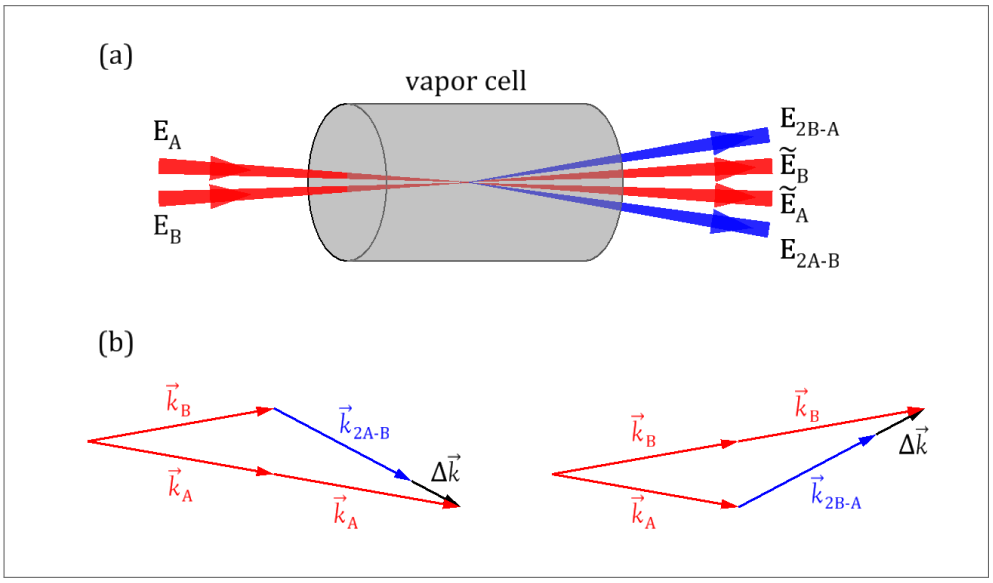

Source: the author (2023).

Our vapor cell contains atomic vapor of $^{85}\mathrm{Rb}$ and $^{87}\mathrm{Rb}$, although we performed our experiment in transitions belonging to $^{85}\mathrm{Rb}$, more specifically, transitions corresponding to the D2 line, from ground level $5^2S_{1/2}$ $(F = 3)$ to excited level $5^2P_{3/2}$. Figure 9 shows the energy levels of $^{85}\mathrm{Rb}$.

Figure 9 – Rubidium 85 D2 transition hyperfine structure, with frequency splittings between the hyperfine energy levels.

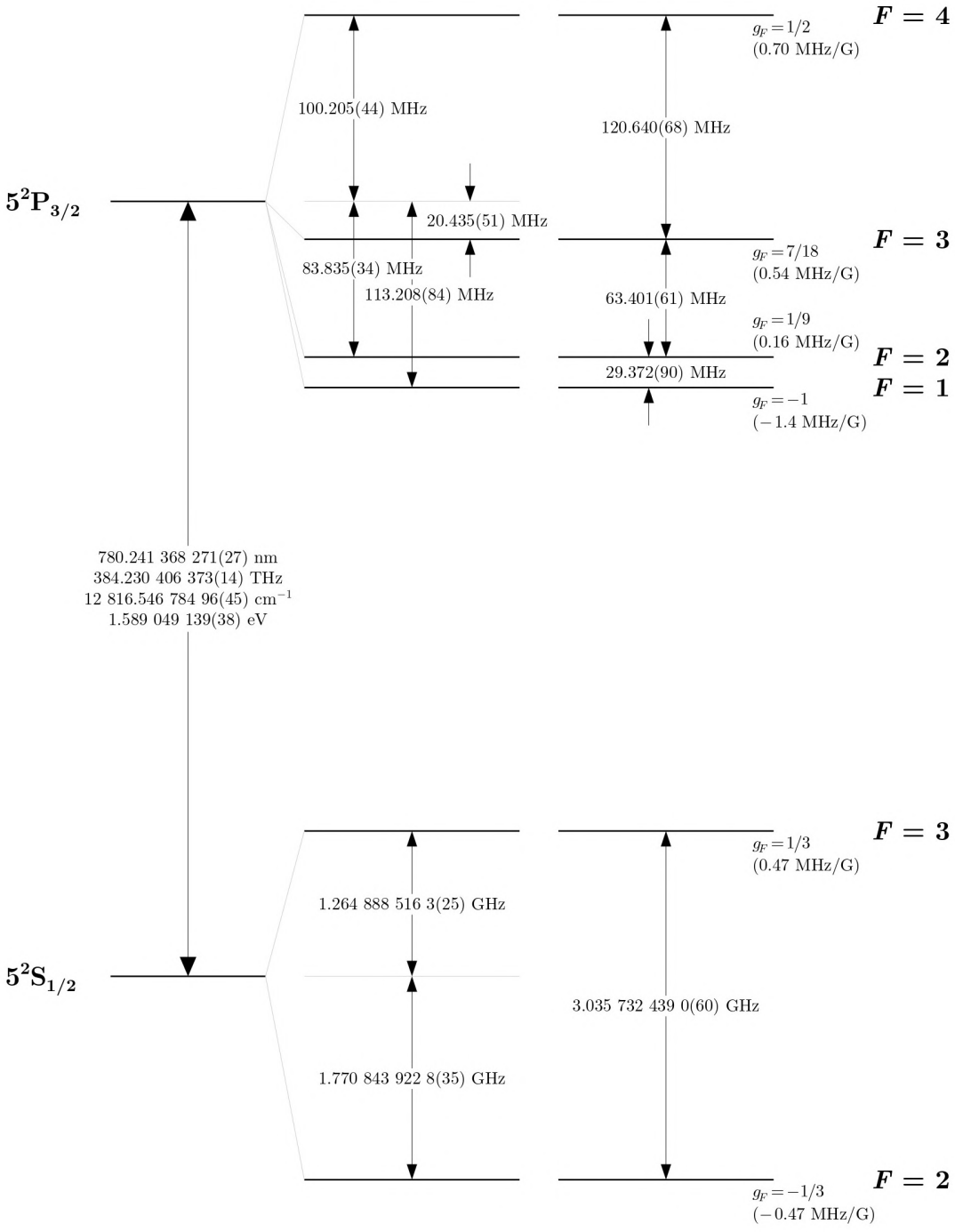

Source: taken from reference [34].

In summary, our experiment is a degenerate four-wave mixing since all the beams involved in the process have the same frequencies. We want to look at the signals generated by the absorption of two photons from A and stimulated emission by a photon from B, and vice-versa. Considering this arrangement, the polarizations of the beams involved occur in pairs, thus signal $2A-B$ has the same polarization as B, and signal $2B-A$ has the same polarization as A. The diagrams in figure 8(b) illustrate the momentum conservation of the process, highlighting the phase mismatch. As discussed in subsection 2.1.1, maximizing efficiency relies on minimizing the phase mismatch, which requires a small angle between the beams. In our experiment, the angle has the purpose of spatially separating the generated signals from the transmitted light of beams A and B. However, from a computational standpoint, there are no drawbacks in making the beams perfectly parallel to each other, nullifying the phase mismatch.

With the assumptions made, we write the polarization induced in our system as

$$\vec{P} = \varepsilon_0\chi^{(1)}(\vec{E}_A + \vec{E}_B + \vec{E}_{2A-B} + \vec{E}_{2B-A}) + 3\varepsilon_0\chi^{(3)}(\vec{E}_A^2\vec{E}_B^* + \vec{E}_B^2\vec{E}_A^*)\,. \tag{3.1}$$

The linear component is responsible for the absorption of the beams by the atomic medium. For the nonlinear terms, the second-order polarization is null since we are treating a centrosymmetric medium, and for the third-order polarization, we write specifically those contributions that generate the nonlinear signals we are interested in. From now on, we will focus on solving the wave equation for the nonlinear polarization $\vec{P}^{(3)}_{2A-B} = 3\epsilon_0\chi^{(3)}\vec{E}_A^2\vec{E}_B^*$, which is responsible for generating the signal $2A-B$. It should be noted that the solution for $2B-A$ can be obtained by analogy, just by reversing the labels.

3.2 SOLUTIONS TO THE PARAXIAL WAVE EQUATION

In this section, we will focus our efforts on solving the wave equation,

$$\nabla^2\vec{E}_{2A-B} - \frac{n^2}{c^2}\frac{\partial^2\vec{E}_{2A-B}}{\partial t^2} = \mu_0\frac{\partial^2\vec{P}^{(3)}_{2A-B}}{\partial t^2}\,. \tag{3.2}$$

First, we apply the manipulation demonstrated in section 2.2, arriving at the inhomogeneous paraxial wave equation,

$$\nabla_\perp^2 u_{2A-B} + 2ik\frac{\partial u_{2A-B}}{\partial z} = -3k^2\chi^{(3)}u_A^2u_B^*\,. \tag{3.3}$$

Now, we use the orthogonality and completeness properties to expand the nonlinear signal envelope in terms of the Hermite-Gauss functions,

$$u_{2A-B}(\vec{r}) = \sum_{m,n}\Lambda_{mn}(z)\mathrm{HG}_{mn}(\vec{r})\,, \tag{3.4}$$

where $\Lambda_{mn}(z)$ is the probability amplitude, representing the contribution coefficient of each mode (m, n), and $u_A(\vec{r})$ and $u_B(\vec{r})$ are pure Hermite-Gauss modes themselves, with modes (m_A, n_A) and (m_B, n_B), respectively,

$$u_\alpha(\vec{r}) = \mathrm{HG}_{m_\alpha n_\alpha}(\vec{r}), \qquad \alpha \in \{A, B\} \, . \tag{3.5}$$

Substitution of (3.4) and (3.5) in equation (3.3) results in

$$\sum_{m,n} \left(\nabla_\perp^2 + 2ik\frac{\partial}{\partial z} \right) \Lambda_{mn}(z)\mathrm{HG}_{mn}(\vec{r}) = -3k^2\chi^{(3)}\mathrm{HG}^2_{m_A n_A}(\vec{r})\mathrm{HG}^*_{m_B n_B}(\vec{r}) \, . \tag{3.6}$$

Distributing the differential operator, and using the fact that $\mathrm{HG}_{mn}(\vec{r})$ is a solution to the homogeneous equation, we arrive at

$$\sum_{m,n} \mathrm{HG}_{mn}\frac{\partial}{\partial z}\Lambda_{mn}(z) = -\frac{3}{2}ik\chi^{(3)}\mathrm{HG}^2_{m_A n_A}(\vec{r})\mathrm{HG}^*_{m_B n_B}(\vec{r}) \, . \tag{3.7}$$

Now, we multiply this equation by $\mathrm{HG}^*_{mn}(\vec{r})$ and integrate it over the transverse plane. Using the orthogonality of the HG functions leads to

$$\frac{\partial}{\partial z}\Lambda_{mn}(z) = -\frac{3}{2}ik \iint \chi^{(3)}\mathrm{HG}^2_{m_A n_A}(\vec{r})\mathrm{HG}^*_{m_B n_B}(\vec{r})\mathrm{HG}^*_{mn}(\vec{r}) \, dxdy \, . \tag{3.8}$$

Considering that our input fields are strong enough to undergo little or no transverse structure variation inside the cell, we uncouple the spatial dependency of $\chi^{(3)}$. Finally, integration over z, results in

$$\Lambda_{mn}(z) = -\frac{3}{2}ik\chi^{(3)} \iiint \mathrm{HG}^2_{m_A n_A}(\vec{r})\mathrm{HG}^*_{m_B n_B}(\vec{r})\mathrm{HG}^*_{mn}(\vec{r}) \, dxdydz \, , \tag{3.9}$$

which we call the overlap integrals of the interacting beams. It can be interpreted as the projection of the generated nonlinear field onto the space of HG functions.

The integrals in x and y are performed over the entire transverse plane. There is no loss of generality when considering experimental conditions where the beam waists are much smaller than the diameter of the cell. Now, for the longitudinal axis, some considerations have to be made, since our cell has a limited length. We integrate over an extension of size L, which represents the length of the vapor cell, centered around the origin. Finally, we write the integrals as

$$\Lambda_{mn}(L) = -\frac{3}{2}ik\chi^{(3)} \int_{-L/2}^{+L/2}\int_{-\infty}^{+\infty}\int_{-\infty}^{+\infty} \mathrm{HG}^2_{m_A n_A}(\vec{r})\mathrm{HG}^*_{m_B n_B}(\vec{r})\mathrm{HG}^*_{mn}(\vec{r}) \, dxdydz \, . \tag{3.10}$$

3.3 OVERLAP INTEGRALS

In this section, we'll focus on solving the overlap integrals (3.10), which will lead to some selection rules that govern the mode transfer. We start by expanding the HG functions inside the integral,

$$\begin{aligned}\Lambda_{mn}(L) = -\frac{6}{\pi} ik\chi^{(3)} C^{n;\,n_A,\,n_B}_{m;\,m_A,\,m_B} \int_{-L/2}^{+L/2}\int_{-\infty}^{+\infty}\int_{-\infty}^{+\infty} \frac{1}{w_A^2(z) w_B(z) w_{2A-B}(z)} \\ \times \exp\left[-(x^2+y^2)\left(\frac{2}{w_A^2(z)} + \frac{1}{w_B^2(z)} + \frac{1}{w_{2A-B}^2(z)}\right)\right] \\ \times \mathrm{H}^2_{m_A}\left[\frac{\sqrt{2}x}{w_A(z)}\right] \mathrm{H}^*_{m_B}\left[\frac{\sqrt{2}x}{w_B(z)}\right] \mathrm{H}^*_{m}\left[\frac{\sqrt{2}x}{w_{2A-B}(z)}\right] \\ \times \mathrm{H}^2_{n_A}\left[\frac{\sqrt{2}y}{w_A(z)}\right] \mathrm{H}^*_{n_B}\left[\frac{\sqrt{2}y}{w_B(z)}\right] \mathrm{H}^*_{n}\left[\frac{\sqrt{2}y}{w_{2A-B}(z)}\right] \\ \times \exp\left[i\frac{x^2+y^2}{2}\left(\frac{2k_A}{R_A(z)} - \frac{k_B}{R_B(z)} - \frac{k_{2A-B}}{R_{2A-B}(z)}\right)\right] \\ \times \exp\left[-2iN_A \tan^{-1}\left(\frac{z}{z_{R\,(A)}}\right) + iN_B \tan^{-1}\left(\frac{z}{z_{R\,(B)}}\right)\right. \\ \left. + iN_{2A-B}\tan^{-1}\left(\frac{z}{z_{R\,(2A-B)}}\right)\right] dxdydz\,.\end{aligned} \tag{3.11}$$

The term $C^{n;\,n_A,\,n_B}_{m;\,m_A,\,m_B} = C^2_{m_A n_A} C_{m_B n_B} C_{mn}$, where C_{jl} is the normalization coefficient of each HG mode (j,l). The parameters k_α, $w_\alpha(z)$, $R_\alpha(z)$ and $z_{R\,(\alpha)}$ of each beam are properly labeled, where $\alpha \in \{A, B, 2A-B\}$.

To evaluate these integrals, we assume that Boyd's criterion [10] holds in our system. It is an empiric criterion that establishes some requirements to maximize signal generation. In short, it states that the Rayleigh length of the beams involved in the process should be the same, which results in the relation:

$$\begin{aligned} z_{R\,(A)} = z_{R\,(B)} = z_{R\,(2A-B)}\,, \\ \frac{w_A^2}{\lambda_A} = \frac{w_B^2}{\lambda_B} = \frac{w_{2A-B}^2}{\lambda_{2A-B}}\,. \end{aligned} \tag{3.12}$$

Since our system is degenerate, the beams also have the same wavelength, which implies that they must have the same waist. After applying these considerations to the overlap integral,

we get the expression,

$$\begin{aligned}\Lambda_{mn}(L) = -\frac{6}{\pi} ik\chi^{(3)} C^{n;\,n_A,\,n_B}_{m;\,m_A,\,m_B} \int_{-L/2}^{+L/2}\int_{-\infty}^{+\infty}\int_{-\infty}^{+\infty} \frac{1}{w^4(z)} \exp\left[-4\frac{x^2+y^2}{w^2(z)}\right] \\ \times \mathrm{H}^2_{m_A}\left[\frac{\sqrt{2}x}{w(z)}\right] \mathrm{H}^*_{m_B}\left[\frac{\sqrt{2}x}{w(z)}\right] \mathrm{H}^*_{m}\left[\frac{\sqrt{2}x}{w(z)}\right] \\ \times \mathrm{H}^2_{n_A}\left[\frac{\sqrt{2}y}{w(z)}\right] \mathrm{H}^*_{n_B}\left[\frac{\sqrt{2}y}{w(z)}\right] \mathrm{H}^*_{n}\left[\frac{\sqrt{2}y}{w(z)}\right] \\ \times \exp\left[-i(2N_A - N_B - N_{2A-B})\tan^{-1}(z/z_R)\right] dxdydz\,.\end{aligned} \tag{3.13}$$

Now, we make the substitution $\tilde{x} = \sqrt{2}x/w(z)$ and $\tilde{y} = \sqrt{2}y/w(z)$, and we may separate the integrals,

$$\begin{aligned}\Lambda_{mn}(L) = -\frac{3}{\pi} ik\chi^{(3)} C^{n;\,n_A,\,n_B}_{m;\,m_A,\,m_B} \int_{-\infty}^{+\infty} \mathrm{H}^2_{m_A}(\tilde{x})\mathrm{H}^*_{m_B}(\tilde{x})\mathrm{H}^*_{m}(\tilde{x}) e^{-2\tilde{x}^2}\, d\tilde{x} \\ \times \int_{-\infty}^{+\infty} \mathrm{H}^2_{m_A}(\tilde{y})\mathrm{H}^*_{m_B}(\tilde{y})\mathrm{H}^*_{m}(\tilde{y}) e^{-2\tilde{y}^2}\, d\tilde{y} \\ \times \int_{-L/2}^{+L/2} \frac{1}{w^2(z)} e^{-i(2N_A - N_B - N_{2A-B})\tan^{-1}(z/z_R)}\, dz\,.\end{aligned} \tag{3.14}$$

3.3.1 Transverse integrals

The transverse integrals are similar to each other, both consisting of a product of Hermite functions and a Gaussian term,

$$I_x = \int_{-\infty}^{+\infty} \mathrm{H}^2_{m_A}(\tilde{x})\mathrm{H}^*_{m_B}(\tilde{x})\mathrm{H}^*_{m}(\tilde{x}) e^{-2\tilde{x}^2}\, d\tilde{x}\,, \tag{3.15}$$

$$I_y = \int_{-\infty}^{+\infty} \mathrm{H}^2_{m_A}(\tilde{y})\mathrm{H}^*_{m_B}(\tilde{y})\mathrm{H}^*_{m}(\tilde{y}) e^{-2\tilde{y}^2}\, d\tilde{y}\,. \tag{3.16}$$

The arguments of these integrals are functions with well-defined parity and are being integrated over a symmetric interval. They are nonzero only when the product of Hermite polynomials is an even function, which occurs when the sum of indexes is an even number,

$$\begin{aligned} 2m_A + m_B + m_{2A-B} &= 2j, \qquad j \in \mathbb{N}\,, \\ 2n_A + n_B + n_{2A-B} &= 2j, \qquad j \in \mathbb{N}\,, \end{aligned} \tag{3.17}$$

which can be unified in a single condition involving the mode order of the beams,

$$2N_A + N_B + N_{2A-B} = 2j, \qquad j \in \mathbb{N}\,. \tag{3.18}$$

We interpret this selection rule as a conservation of parity, where the parity of the generated signal is equal to the parity of the product of the incident beams. More specifically, since beam A participates twice in the process, its contribution is nullified, and the parity of the nonlinear signal is always determined by the parity of beam B,

$$N_B + N_{2A-B} = 2j, \qquad j \in \mathbb{N}\,. \tag{3.19}$$

We emphasize that this result holds without making any assumptions about the length of the medium. Therefore, it is valid for both cases when the medium is short compared to the Rayleigh length of the beam, as well as when the medium is long compared to the Rayleigh length of the beam.

3.3.2 Longitudinal integrals

The longitudinal integral is expressed as

$$I_z = \int_{-L/2}^{+L/2} \frac{e^{-i(2N_A - N_B - N_{2A-B})\tan^{-1}(z/z_R)}}{1 + (z/z_R)^2}\, dz\,. \tag{3.20}$$

It is important to note that the contribution of the longitudinal phase, resulting from the curvature radius, has been nullified by Boyd's criterion. As a result, only dependence on the Gouy phase remains. Using the identity

$$e^{-i\tan^{-1}(z/z_R)} = \cos\left[\tan^{-1}(z/z_R)\right] - i\sin\left[\tan^{-1}(z/z_R)\right], \tag{3.21}$$

and taking the triangle of figure 10 as a guide, we are able to rewrite the integral in the form

$$I_z = \int_{-L/2}^{+L/2} \frac{1}{1 + (z/z_R)^2} \left[\frac{1 - iz/z_R}{\sqrt{1 + (z/z_R)^2}}\right]^{\Delta N} dz\,, \tag{3.22}$$

where $\Delta N = 2N_A - N_B - N_{2A-B}$ is the variation of mode order.

Figure 10 – Right triangle with angle $\varphi = \tan^{-1}(z/z_R)$.

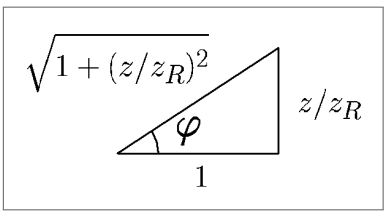

Source: the author (2023).

This integral can be analytically evaluated and results in

$$I_z = \begin{cases} 2z_R \tan^{-1}(L/2z_R)\,, & \text{if } \Delta N = 0\,; \\ \dfrac{iz_R}{\Delta N}\left[\left(\dfrac{i+L/2z_R}{i-L/2z_R}\right)^{\Delta N/2} - \left(\dfrac{i+L/2z_R}{i-L/2z_R}\right)^{-\Delta N/2}\right], & \text{if } \Delta N \neq 0\,. \end{cases} \tag{3.23}$$

This solution yields different results when considering the cases of a thin or extensive medium, which are related to the Gouy phase matching.

In the thin medium case, $z_R/L \gg 1$, and we obtain

$$\lim_{z_R/L \gg 1} I_z = L, \qquad \forall\ \Delta N\,. \tag{3.24}$$

In this limit, the medium is short in comparison to the Rayleigh length of the beam, which means that it accumulates a negligible Gouy phase during the propagation inside the medium. As a result, modes that don't necessarily satisfy the Gouy phase matching end up contributing significantly to the nonlinear signal.

Now, in the extensive medium case, $z_R/L \ll 1$, and we get

$$\lim_{z_R/L \ll 1} I_z = \begin{cases} \pi z_R, & \text{if } \Delta N = 0\,; \\ 0, & \text{if } \Delta N \neq 0\,. \end{cases} \tag{3.25}$$

In this limit, the medium is long in comparison to the Rayleigh length of the beam, which means that it accumulates a significant Gouy phase during the propagation inside the medium. Consequently, the modes that contribute to the nonlinear signal are those that satisfy Gouy phase matching. The selection rule, $\Delta N = 0$, is valid only in the extensive regime and explicitly represents the conservation of mode order,

$$N_{2A-B} = 2N_A - N_B\,. \tag{3.26}$$

4 THE EXPERIMENT

In this chapter, we intend to describe our experiment, pointing out key instruments and describing the procedures performed in our measurements. First, we describe our experimental setup, then we detail the functionality of the spatial light modulator (SLM) and how we control it. We finish by describing the method we use to take our measurements and how we proceed to process our images.

4.1 EXPERIMENTAL SETUP

Our system is composed of a laser, mirrors, beam splitters, fibers, an SLM, and other optical components. Figure 11 shows the main structure of the experimental setup we are gonna be describing in the next lines. For the experiment, we used a diode laser from Sanyo, model

Figure 11 – Experimental setup.

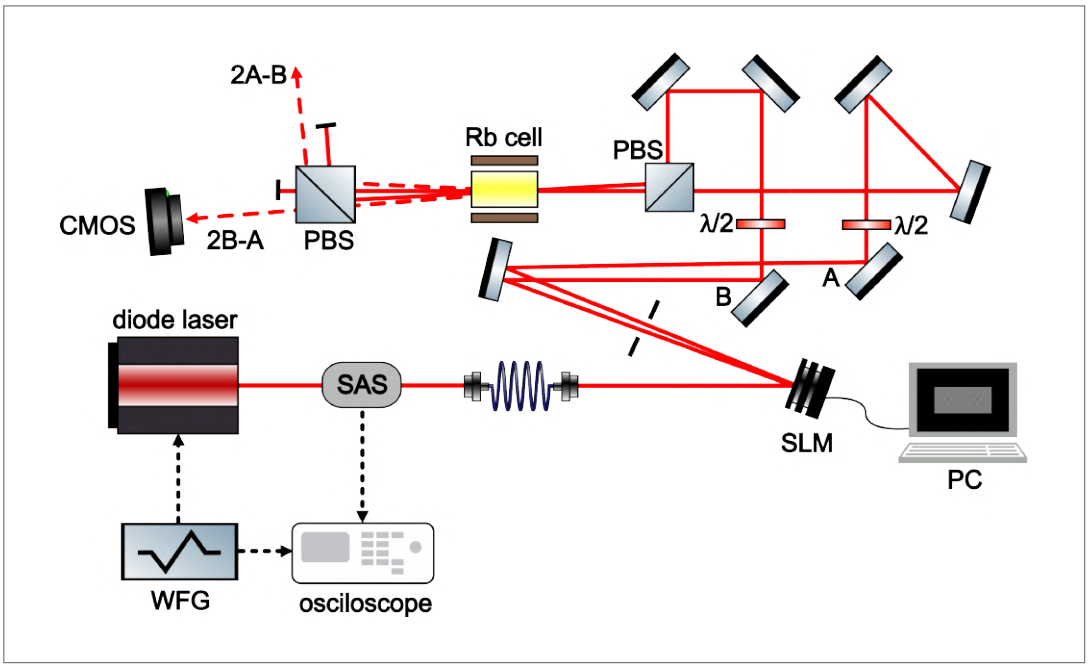

Source: the author (2023).

DL7140-201S, at wavelength $\lambda = 780\ \mathrm{nm}$, with homemade electronics, for temperature and current control. The laser's frequency is modulated using a waveform generator (WFG) from Agilent, model 33521A. The first part of the system is a saturated absorption spectroscopy (SAS) arrangement. This first part of the experiment is important, so we can tune the frequency of the laser to the desired transition. It will be detailed in the next subsection.

As the beam is emitted by the laser, it has a messy shape that doesn't resemble a Gaussian profile. So, to clear its appearance, we pass the beam through an optical fiber right after the SAS. Once it exits the fiber, the beam has an almost perfect Gaussian shape, aside from some subtle interference. Figure 12 shows a comparison between the profiles of the beam before and after it goes through the optical fiber. Then we direct the beam to an SLM, which we use to

Figure 12 – Comparison between the beam profile (a) before and (b) after the optical fiber.

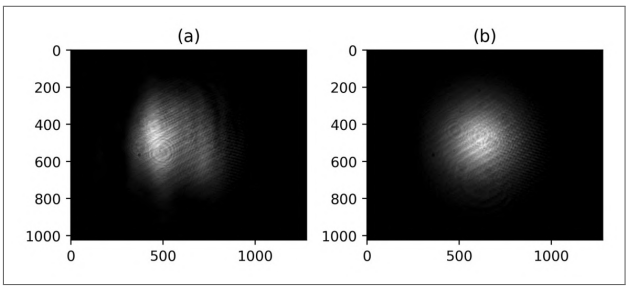

Source: taken from reference [35].

divide the beam in two, A and B, and shape them in the desired Hermite-Gauss modes. As the beams propagate, they separate, and with the use of half-wave plates, we adjust them with linear and orthogonal polarizations. The beams meet in a polarizing beamsplitter (PBS) and cross their paths further ahead inside a rubidium vapor cell that is heated to approximately $72\,^{\circ}\mathrm{C}$. For this, we use a heater for glass cells and a temperature controller, both from Thorlabs, models GCH25-75 and TC200, respectively. The interaction of the two beams, A and B, with wavevectors $\vec{k}_A$ and $\vec{k}_B$, with the atomic medium generates two four-wave mixing signals, at directions $2\vec{k}_A - \vec{k}_B$ and $2\vec{k}_B - \vec{k}_A$. After the Rb cell, we separate the beams by polarization using a PBS and then further isolate them mechanically by blocking the transmitted beams. We align the system to detect one of the signals, using a CMOS camera.

4.1.1 Saturated absorption spectroscopy setup

In this subsection, we detail the SAS system in our experiment. Saturation spectroscopy is a powerful technique that allows us to eliminate the Doppler effect and then, precisely measure the energy levels and transitions of an atomic or molecular sample. Figure 13 illustrates our SAS arrangement. First, we pass the beam through an optical isolator that will prevent reflected light from returning to the laser head. Next, we deflect a few Watts of power using a non-polarizing beamsplitter (a simple thin glass plate). The light deflected passes through a rubidium cell at room temperature and reflects back on itself passing through a neutral density

Figure 13 – Saturated absorption spectroscopy setup.

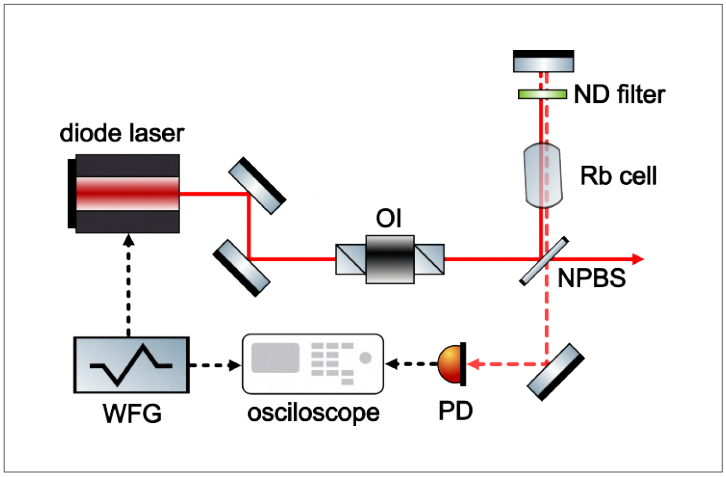

Source: the author (2023).

(ND) filter twice. This way two beams are passing through the sample, one of them with much greater intensity. The reflected weaker beam is collected using a simple photodetector. This arrangement depends on both the beams passing through the sample over each other. Due to the Doppler effect, this technique will involve the excitation of different velocity groups by each one of the beams, separately, except when the beams are tuned to the resonant frequency. In the resonance condition, the two beams, which propagated in opposite directions, interact with the same atoms that, in this case, are at rest, $v = 0$. The stronger beam will saturate the transitions while the weaker beam, which we call probe beam, will be less absorbed. We detect the probe beam, which will exhibit large absorption lines, corresponding to the fine structure of the atoms, and thinner transmission lines carved over the absorption lines, at the resonant frequencies, corresponding to the hyperfine structure of the atoms.

Another interesting property of this technique is the occurrence of spurious peaks that don't correspond to real transitions, but to *crossovers* of the resonant frequencies. When the lasers are tuned to the mean of two resonant frequencies, $\omega_{\mathrm{CO}} = (\omega_1 + \omega_2)/2$, atoms with velocity $v = \pm(\omega_2 - \omega_1)/2k$ will feel each beam tuned to one of the resonant frequencies. The pump beam will saturate the transitions to one of the excited levels, and the probe beam, which is resonant to the other transition, will be transmitted. This mechanism carves another peak inside the Doppler profile, which is usually greater than the transition peaks, due to being the result of the interaction of the laser with atoms belonging to two velocity groups. Figure 14 illustrates the mechanism of the crossover peaks.

The saturated absorption spectrum can be used as a reference to control the frequency of

Figure 14 – (a) Energy levels of a three-level system illustrating the crossover frequency. (b) The spectrum of the probe beam will exhibit an intermediate peak between the resonant frequencies.

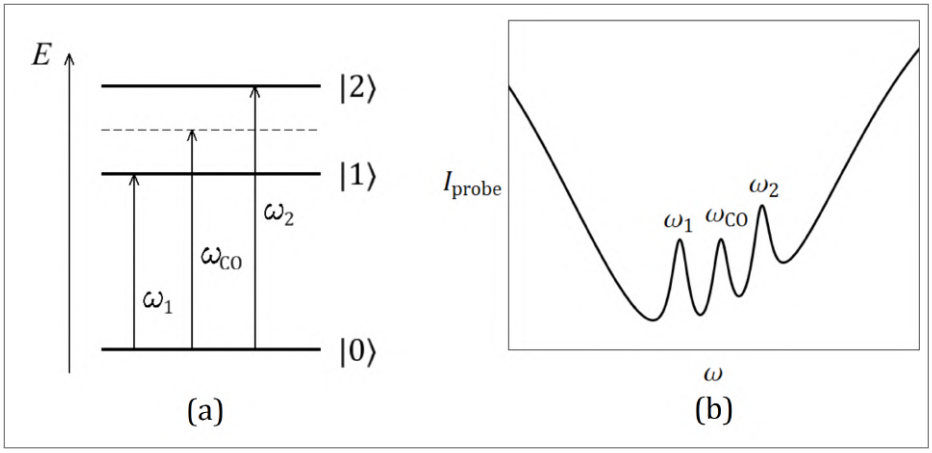

Source: the author (2023).

the laser. We use it basically as a frequency ruler. Figure 15 shows the spectrum of the saturated spectroscopy in our system. The bigger plot shows four Doppler profiles corresponding to the fine structure of $^{85}\mathrm{Rb}$ and $^{87}\mathrm{Rb}$, each containing inner peaks that correspond to the hyperfine structure, half of them are transitions and the other half are crossovers. In the inset plot, we zoom in to highlight the structure of the $^{85}\mathrm{Rb}$ $(F_g = 3)$ Doppler line, because it's the range of frequencies in which we performed our measurements.

Figure 15 – Saturated absorption spectrum of Rubidium in our system. The inset graph is a zoom of the $^{85}\mathrm{Rb}$ $(F_g = 3)$ Doppler curve.

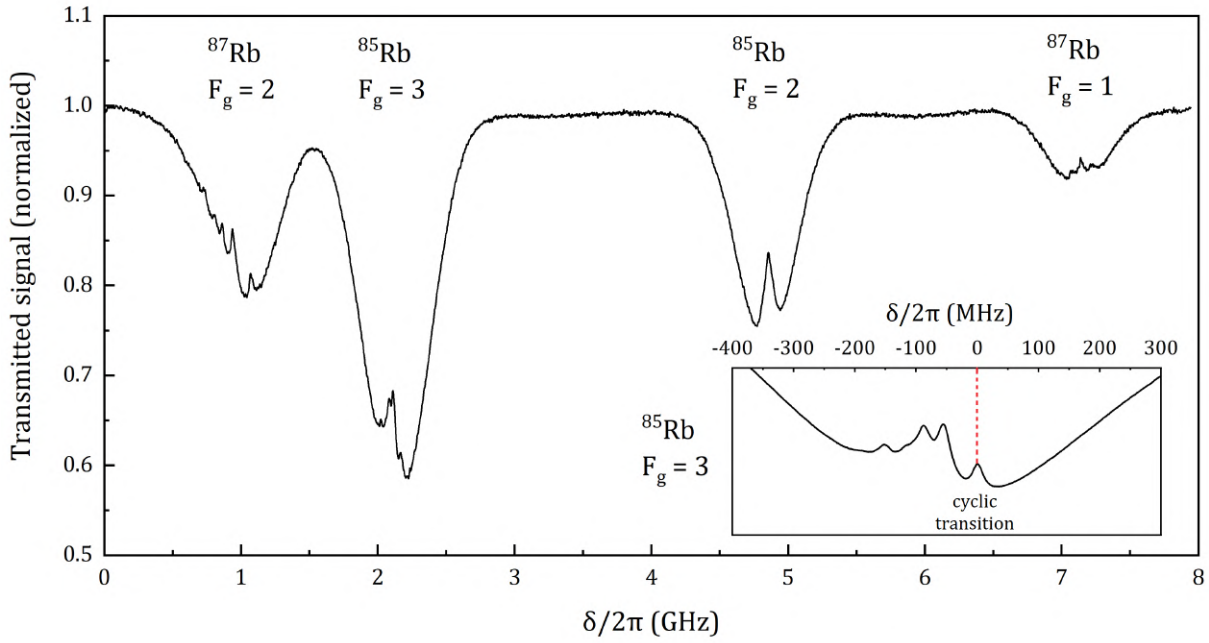

Source: the author (2023).

4.2 SPATIAL LIGHT MODULATOR

In this work, we use an LCOS-SLM (liquid crystal on silicon spatial light modulator) from Hamamatsu Photonics, model X10468-02. A liquid crystal spatial light modulator is a device used to modulate the phase of an incident wavefront [36]. The chip is composed of a silicon base with pixels, made of aluminum electrodes. This substrate is covered by a layer of nematic liquid crystal and the whole ensemble is protected by a glass plate. An incident laser beam should pass through the glass plate and interact with the liquid crystal (LC), before being reflected. The LC molecules present an elongated ellipsoidal shape and the property of birefringence. The transversal axes of the crystal hold the same refractive index, which we call ordinary, n_o, whilst the longitudinal axis holds an extraordinary refractive index, n_e.

Figure 16 – (a) LCOS-SLM inner structure and peripheral devices. (b) Representation of a liquid crystal molecule, highlighting its refractive indexes in each axis.

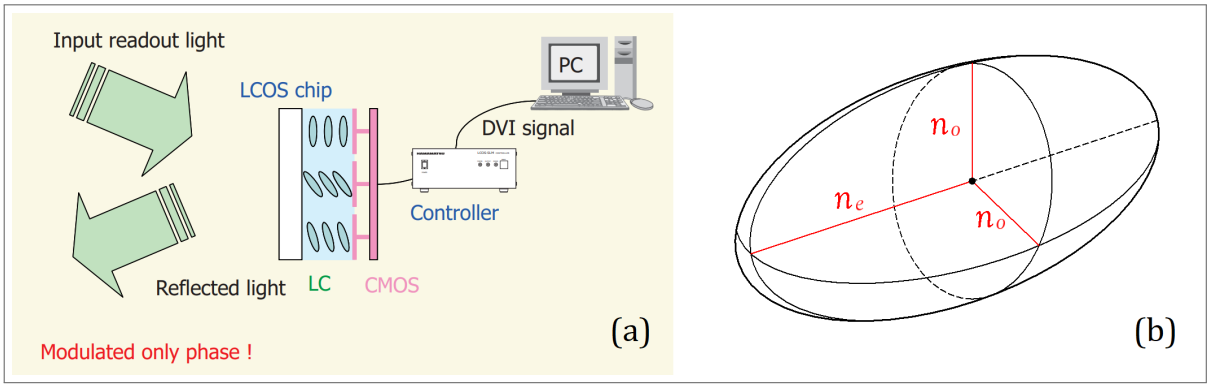

Source: (a) taken from the SLM manual [37] and (b) the author.

The orientation of the liquid crystal molecules is controlled by applying a voltage to each pixel of the display. This can be done with high precision using a computer connected to the controller through a digital video interface signal. In this way, with a Python program, we generate a graphical user interface containing a built mask, where the phase ranging from 0 to 2π is converted to an 8-bit scale (discretely ranging from 0 to 255) in bitmap format. Each level corresponds to a voltage intensity applied to a pixel of the display, which modulates the alignment of the crystals and results in a two-dimensional refractive index distribution.

4.2.1 Generation of higher-order modes

To generate higher-order modes in light beams, we must input masks on the SLM containing the phase profile we want to imprint on the wavefront. This, together with a diffraction grating, is capable of generating beams with high efficiency and a high degree of purity in the desired modes, in the first diffraction order [38]. Figure 17 shows the composition of the phase profile and diffraction grating to generate a HG_{01} mode. In this case, the phase profile adds a shift of π rad in the phase between the top and the bottom hemispheres of the diffraction grating.

Figure 17 – Composition of the mask to generate a HG_{01} mode.

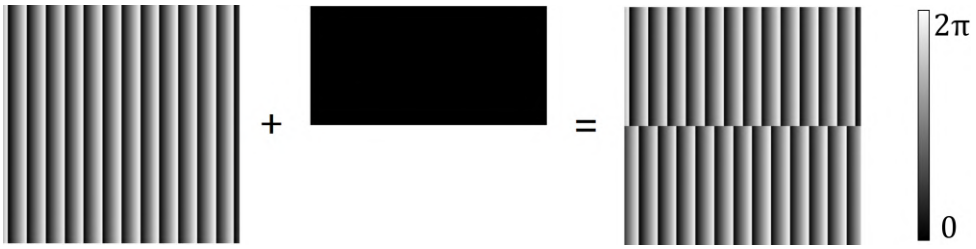

Source: the author (2023).

This can be further perfected by encoding amplitude modulation onto the SLM. There are some different ways to modulate the amplitude of the beam [39, 40], one of the simplest techniques is to obtain an arbitrary combination of amplitude and phase modulation, based on spatially changing the diffraction efficiency [41]. The basic idea is to spatially modulate the phase depth encoded on the hologram (before, fixed at 2π) as the amplitude profile of the mode we want to obtain, in this case, $|\mathrm{HG}_{01}|$. This allows us to control the amount of light reaching the first diffraction order, effectively deflecting undesired light. Figure 18 illustrates this proceeding.

Figure 18 – Amplitude modulation encoding onto the HG_{01} mask.

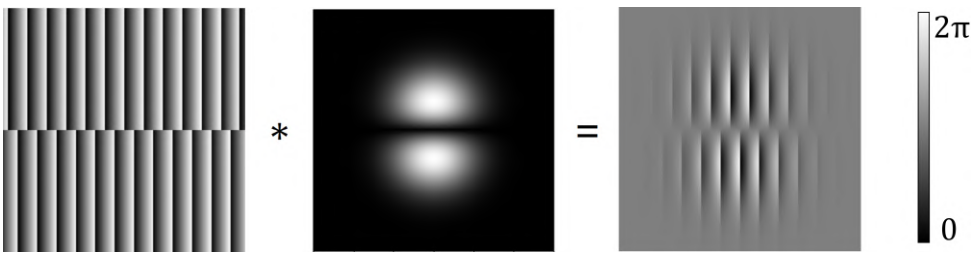

Source: the author (2023).

In our system, we use masks with double holograms, to simultaneously divide our laser beam in two and modulate their shape and phase. Figure 19 shows some examples of masks we use and the resulting beams we get from them.

Figure 19 – (a) Example of masks used in our system and (b) their resulting beams.

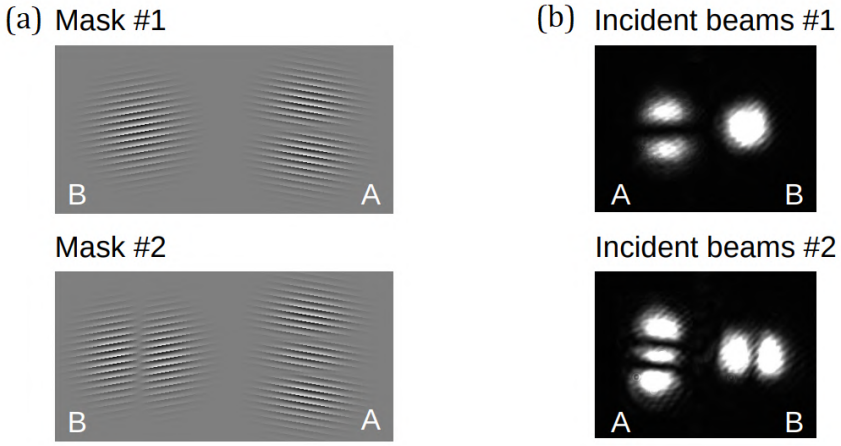

Source: the author (2023).

4.3 MEASUREMENTS

In this section, we provide details about our measurement process and how we proceed with the processing of the recorded images. In this work, we use a CMOS (complementary metal-oxide-semiconductor) camera from Thorlabs, model DCC1545M, shown in Figure 20. It has a resolution of 1280 x 1240 pixels and sensitive dimensions of 6.656 x 5.325 mm.

Figure 20 – CMOS camera, model DCC1545M.

Source: taken from the camera manual [42].

For the measurement, we limit the sweeping range of the laser to the $^{85}\mathrm{Rb}$ $(F = 3)$ Doppler curve, and take a short video of the observed signal as it appears to get stronger

(when the laser approaches the transitions) and faded (when the laser moves away from the resonance). We can notice that the background of the signal presents some scattered light from the transmitted beams, which we also record separately to further clean the image of the signals. We proceed with our measurements in the order described:

1. Record a short video of the nonlinear signal;
2. Block the incident beam A and record a short video of the scattered light from the beam B;
3. Block the incident beam B and record a short video of the scattered light from the beam A.

Then, we follow with the cleaning of the background of the signals:

4. Separate the frames from the videos recorded;
5. Select the best frame from the video of the nonlinear signal;
6. Select the best frames from the videos of the scattered light, the ones which best resemble the background of the nonlinear signal;
7. Subtract the scattered light from the signal image.

Figure 21 follows as an example of the measurement of a Gaussian signal and cleaning of the scattered light.

Figure 21 – Example of measurement and cleaning of the image. In (a) is the chosen frame of the observed nonlinear signal with scattered light, (b) and (c) are the chosen frames of the scattered light from beams A and B, respectively, and (d) is the result of the subtraction of the scattered light from the nonlinear signal.

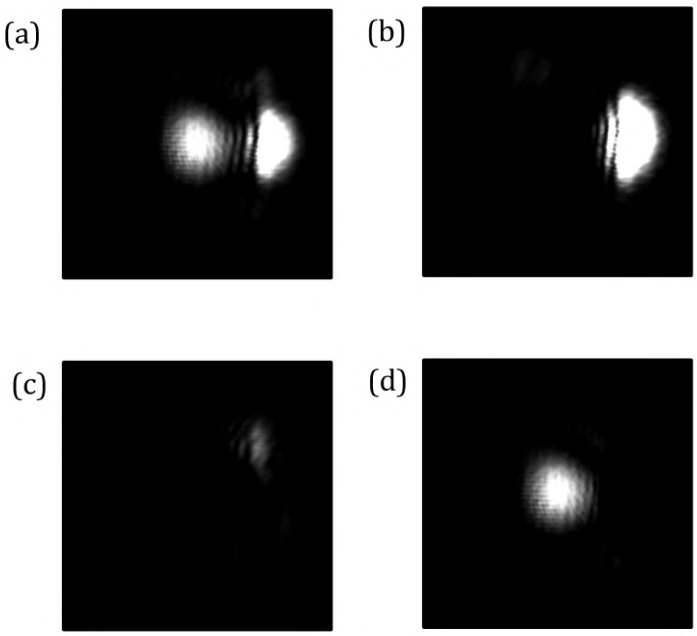

Source: the author (2023).

Next, we apply a color gradient to our image that allows a better evaluation of the intensity profile of the beam. The color gradient has lower-level colors that delimit the boundary of the beams and higher-level colors that give a better perspective on the intensity layers. See figure 22.

Figure 22 – Comparison between (a) the grayscale gradient and (b) the color gradient applied to the signal presented in Figure 21(d).

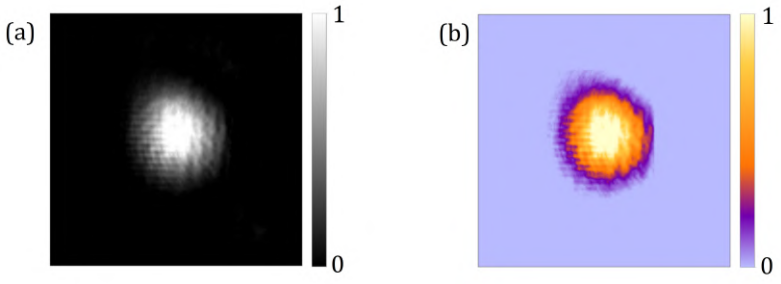

Source: the author (2023).

We further improve our image by removing interference patterns from the beam, arising from the propagation through thin layers, such as lenses, filters, and glass plates, and from direct interference with scattered light. To do this, we perform an averaging procedure in clusters of pixels of the image. We define a parameter ℓ, and a cluster as the square of side $2\ell + 1$ around a pixel of the image, as shown in figure 23. The intensity of the central pixel is redefined as the average intensity of the pixels inside the square. By doing this with each pixel we obtain a smoother image, free from rough interference fringes.

Figure 23 – Illustration of the averaging method. The image represents a 20 x 20 image that will be averaged with a parameter $\ell = 4$. The red square represents the central pixel of the cluster, highlighted as the surrounding yellow squares.

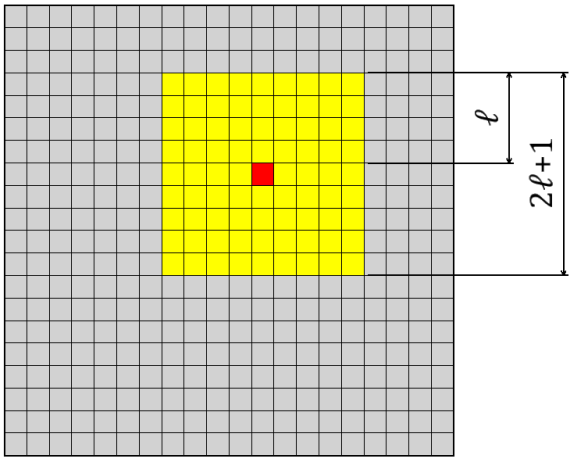

Source: the author (2023).

Figure 24 shows the averaging procedure in the image from figure 22(b), with different values for the parameter ℓ. For the measurements we did in this work, we usually perform the averaging with a parameter ℓ ranging from $\ell = 10$ to $\ell = 15$.

Figure 24 – Comparison between the smoothing of the signal image for different values of the parameter ℓ.

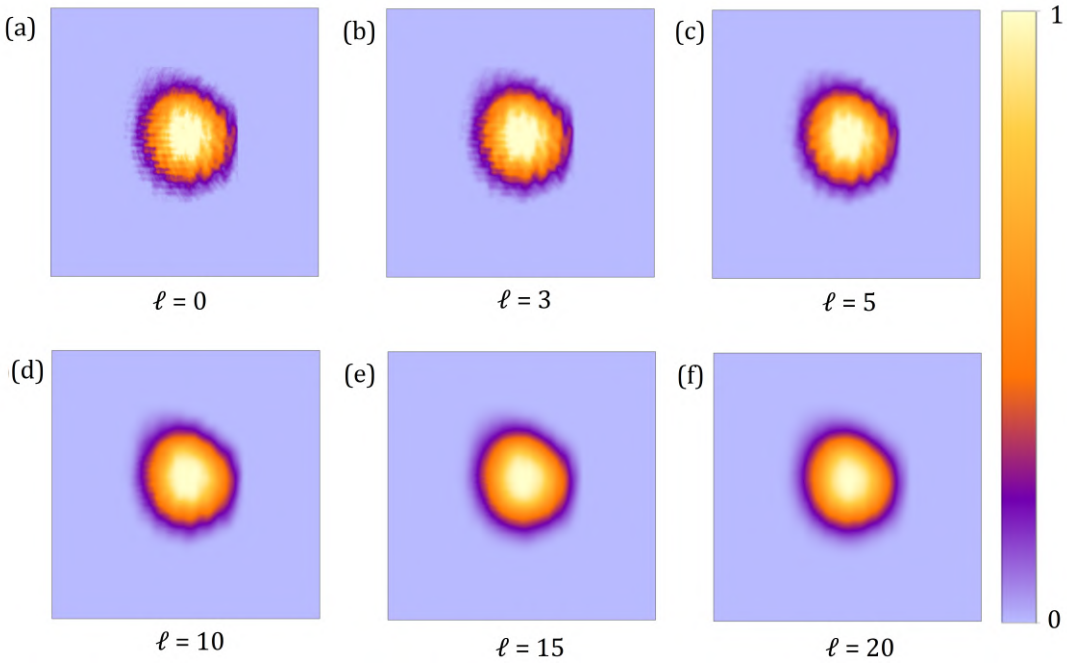

Source: the author (2023).

5 RESULTS

In this chapter, we present and compare our experimental and theoretical results. The chapter is divided into sections, each focusing on a specific thickness regime. We provide a detailed description of the setup and conditions required to achieve these regimes and showcase the transverse profiles we measured together with their corresponding theoretical profiles.

5.1 THIN MEDIUM REGIME

To achieve the thin medium regime, we need an interaction length (length of the cell) much smaller than the Rayleigh length of the beam, $z_R/L \gg 1$. Our cell has a length of approximately $L = 7\ \mathrm{cm}$, and we set the waist of the beams to $w_0 \approx 250\ \mu\mathrm{m}$, giving a Rayleigh length of $z_R \approx 25\ \mathrm{cm}$, therefore a ratio $z_R/L \approx 3.57$. For the FWM setup, we align the beams using guide masks (GMx), consisting of small square copper plates with holes, where the beams pass through, separated by 2 mm intervals, as shown in Figure 25(b). We enumerate the holes on the guide masks from 1 to 4, from left to right. Then, we align beam A to holes 2 and 3 of GM1 and GM2, respectively. On the other hand, we align beam B to holes 3 and 2 of GM1 and GM2, making them cross in the middle, where the rubidium cell is located. The masks are spaced at a distance of $60\ \mathrm{cm}$ from each other, resulting in a small angle between the beams (around $0.007\ \mathrm{rad}$). Signal $2A - B$ is expected to be approximately aligned to holes 1 (GM1) and 4 (GM2), and signal $2B - A$ to holes 4 (GM1) and 1 (GM2).

Figure 25 – (a) Scheme of the beams crossing each other inside the cell. (b) Sketch of the guide masks used to align the beams.

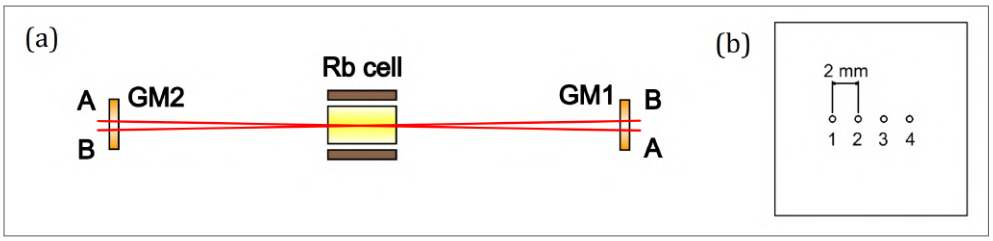

Source: the author (2023).

With this configuration, we obtained measurements for some combinations of Gaussian-HG and HG-HG modes. In Figure 26, we show the profile of the modes we combined in the Gaussian-HG case and their corresponding superposition within the cell. It is important to note that higher-order beams exhibit a greater spread, making it more challenging to achieve overlap

and resulting in increased scattered light. Therefore, we imposed a limit on the maximum mode order of the incident beam, setting it to $N = 2$. Figures 27, 28 and 29 illustrate the results for each combination case, Gaussian-HG, HG-HG (with $u_A = u_B$) and HG-HG (with $u_A \neq u_B$).

Figure 26 – Intensity distribution of the incident beams used to perform the experiment in the gaussian-HG case, and their overlap in the position of the cell.

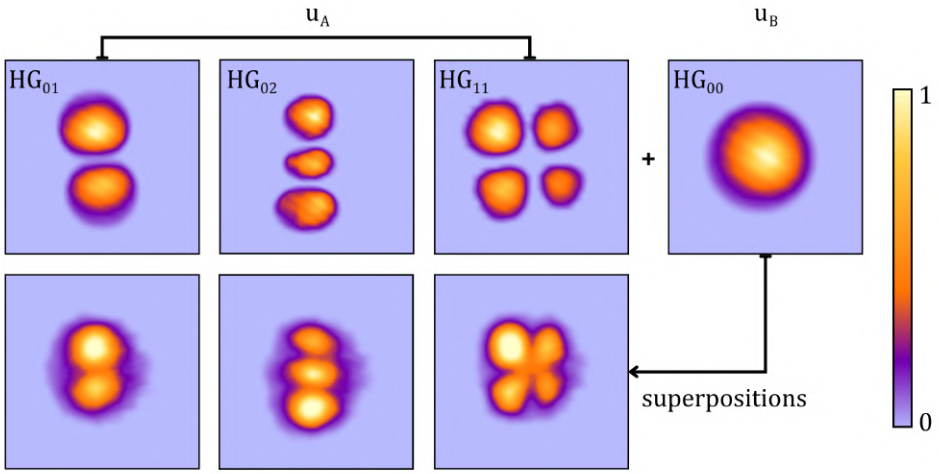

Source: the author (2023).

Figure 27 – Intensity profile for a combination of gaussian-HG modes in the thin medium regime. Here, we show the intensity distribution of the incident u_A beams (u_B is gaussian in every case), and a comparison between the theoretical and experimental distribution of the nonlinear signals.

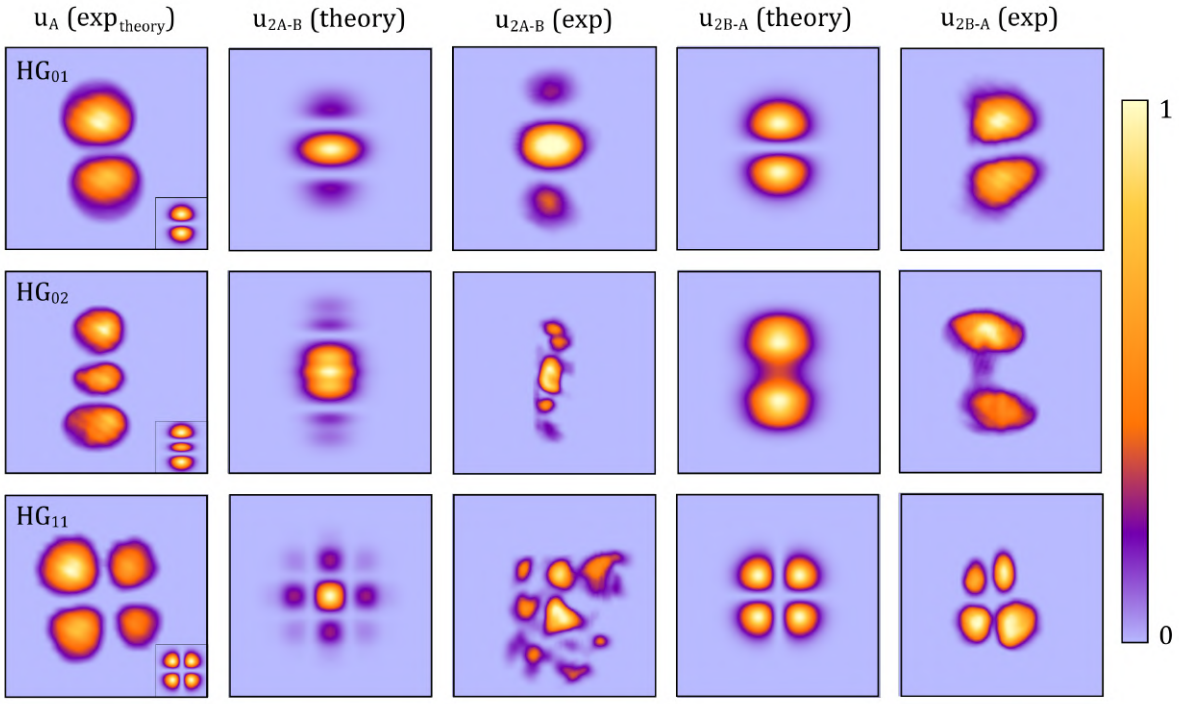

Source: the author (2023).

Figure 28 – Intensity profile for a combination of HG-HG modes, with $u_A = u_B$, in the thin medium regime. Here, we show the intensity distribution of the incident beams and a comparison between the theoretical and experimental distribution of the nonlinear signals.

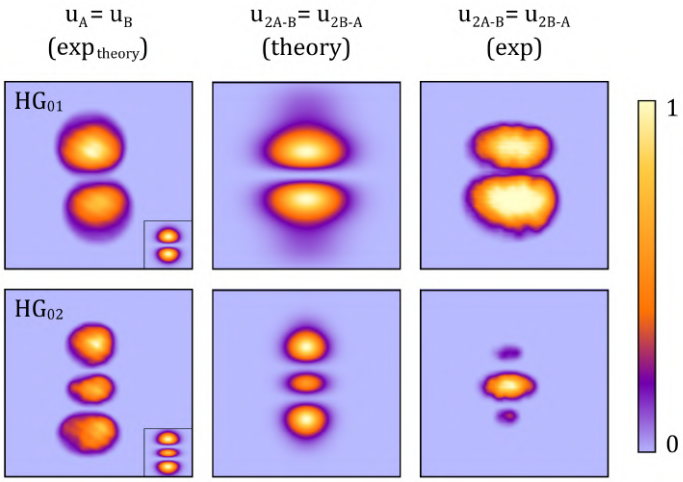

Source: the author (2023).

Figure 29 – Intensity profile for a combination of HG-HG modes, with $u_A \neq u_B$, in the thin medium regime. Here, we show the intensity distribution of the incident beams and a comparison between the theoretical and experimental distribution of the nonlinear signals.

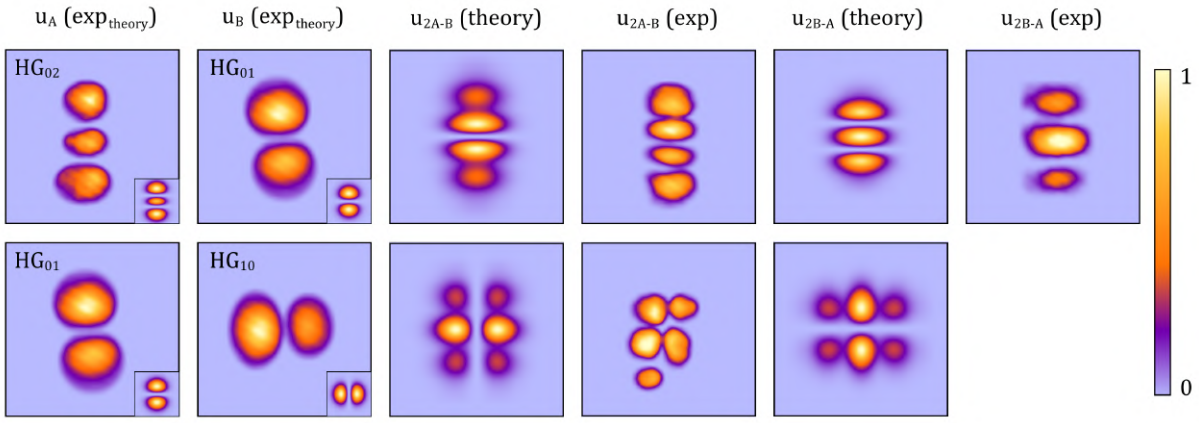

Source: the author (2023).

In general, we observe a good agreement between our experimental and theoretical results in terms of the number of lobes in the nonlinear signals. However, some discrepancies are apparent in their relative intensities, which we attribute mostly to a poor overlap of the beams. Notably, the signal $2A - B$ resulting from the combination of $u_A = \mathrm{HG}_{01}$ and $u_B = \mathrm{HG}_{10}$, in figure 29, is missing a lower right lobe, and we were not able to measure the signal $2B - A$ from the same combination. Another aspect to consider regarding our theoretical model is that we have not accounted for linear effects, which was done in detail by Motta in [43]. His calculations demonstrate that the linear terms lead to absorption, which he represents as an

efficiency term that may depend on the mode indices. In his work, he simplifies the analysis by neglecting this dependence, but the inclusion of this efficiency factor with mode dependence could rearrange the relative contributions of the modes to the nonlinear signals, resulting in a more accurate resemblance between the theoretical and experimental profiles.

5.2 EXTENSIVE MEDIUM REGIME

Firstly, we justify the use of the term "extensive medium" as opposed to the terminology found in the literature, "thick medium", to avoid ambiguities with respect to different concepts. "Thick medium" often refers to media with high optical depth, meaning a high atomic density, which results in greater light absorption. On the other hand, the "extensive medium" regime we are referring to regards the length of the medium in relation to the beam's Rayleigh length, which characterizes its divergence. To achieve the extensive medium regime, we need an interaction length much bigger than the Rayleigh length of the beam, $z_R/L \ll 1$. We recall the length of the cell, $L = 7$ cm, and we were able to set the waist of the beam to $w_0 \approx 50$ μm, giving a Rayleigh length of $z_R \approx 1$ cm, therefore a ratio $z_R/L \approx 0.14$. To obtain this regime, we tried using two different setups, illustrated in figure 30.

Figure 30 – Setups used to obtain the extensive regime. In the first setup (a) we focus both incident beams with a lens. In the second setup (b) we focus only beam A while keeping beam B wide.

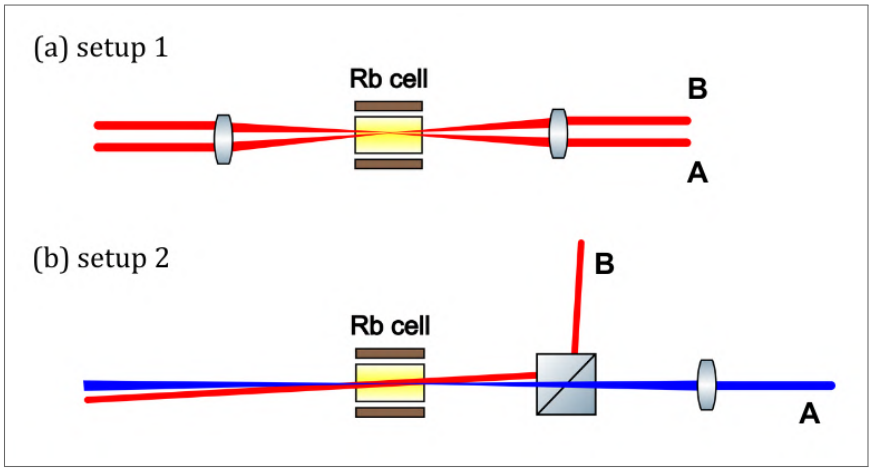

Source: the author (2023).

In the first setup, we align the beams in parallel to each other. Using a lens, we then make the beams cross each other while focusing at the center of the cell. The issue with setup 1 is that the interaction between the two beams occurs within a very small length and volume. As a result, the effective ratio z_R/L is not what was expected (we can't assure we are in the

extensive regime), and the efficiency of the process is reduced due to the participation of a limited number of atoms in the nonlinear process. It is important to note that the intensity of the signal is proportional to the square of the number of atoms, $I \propto N^2$. In the second setup, we focus only beam A by using a lens before the beams meet in the PBS. We keep the beam B wide so that beam A passes through it along the entire length of the cell. In addition to the reduced volume of interaction between the beams, the issue with setup 2 is that it does not meet Boyd's criteria for maximizing efficiency. By adjusting the beams to have different waists, we also create a significant mismatch in their Rayleigh lengths. Unfortunately, we were unable to obtain experimental results for the extensive medium case. However, we will present theoretical results and compare them with the thin medium case.

We start by presenting the first case in detail, in order to analyze every aspect of the phenomenon and the consequences of the selection rules. Figure 31 shows the modes of incident beams A and B for the case of a gaussian-HG combination.

Figure 31 – Input modes of the incident beams A and B.

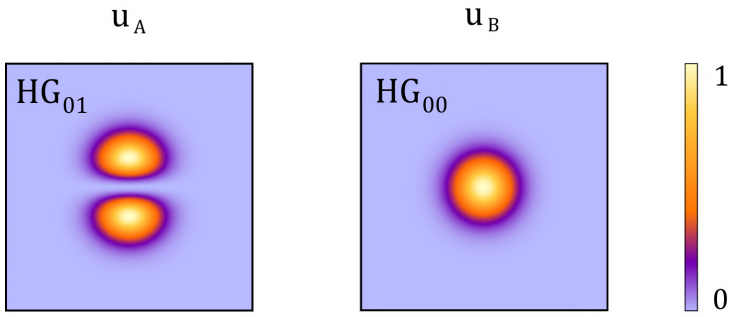

Source: the author (2023).

In this case, where $u_A = \mathrm{HG}_{01}$ and $u_B = \mathrm{HG}_{00}$, their respective mode orders are $N_A = 1$ and $N_B = 0$. The longitudinal selection rule, which is valid in the extensive medium regime, predicts the conservation of mode orders of the nonlinear signals. Therefore, in this regime, we should expect $N_{2A-B} = 2N_A - N_B = 2$ and $N_{2B-A} = 2N_B - N_A = -1$. Hermite functions are defined for positive integers only, so the negative indices solutions predicted for the $2B-A$ signal are not physically possible. This occurs for every combination of gaussian-HG modes in the extensive medium regime, only the signal $2A - B$ is generated.

Figure 32 shows the resulting nonlinear signal $2A - B$ from the combination of incident beams shown in figure 31, in each thickness regime. The black and white diagrams illustrate the numerical values of the coefficients Λ_{mn} theoretically calculated in (3.10). It should be

Figure 32 – Transverse profiles and mode composition of the nonlinear signal $2A - B$ in the extensive and thin medium regimes, considering the incident beams from figure 31.

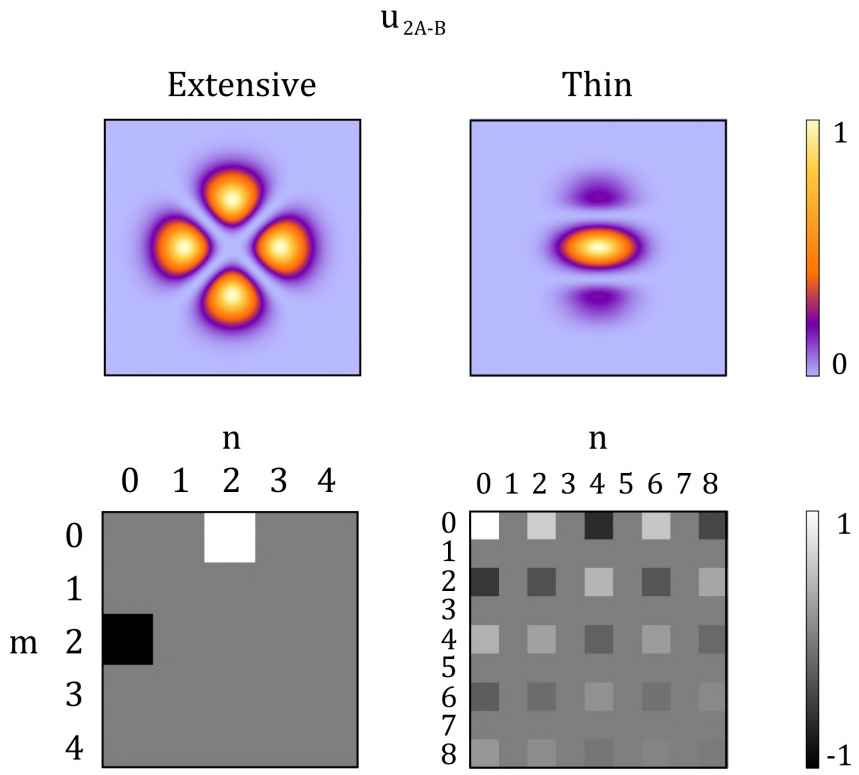

Source: the author (2023).

immediately noticed the difference between the number of modes contributing to each case. In the extensive regime, the conservation of mode order ($N_{2A-B} = 2N_A - N_B = 2$) limits the contribution of modes belonging to a single diagonal of the diagram, containing only modes with order $N = 2$, while in the thin medium regime, a wide range of mode orders arise as contributing to the nonlinear signal. The only simplification we get in the thin regime is related to the conservation of parity of the modes involved ($m_B + m = 2j$ and $n_B + n = 2j$, $j \in \mathbb{N}$), nullifying those with odd indexes m and n. From these diagrams, we can write the solutions of the nonlinear signals as $u_{2A-B}^{extensive} = 0.707\,\mathrm{HG}_{02} - 0.707\,\mathrm{HG}_{02}$ and $u_{2A-B}^{thin} = 0.053\,\mathrm{HG}_{00} + 0.019\,\mathrm{HG}_{02} - 0.019\,\mathrm{HG}_{20} - 0.025\,\mathrm{HG}_{04} - 0.007\,\mathrm{HG}_{22} + 0.008\,\mathrm{HG}_{40} + \cdots$.

It's interesting to notice that our theoretical results align with the conclusions obtained by Offer et al. [25]. Their investigation of a cascade four-wave mixing with Laguerre-Gauss modes showed that the transition from a thin medium to an extensive medium regime led to a reduction in the variety of modes contributing to the generated signals. Although their system shows a more pronounced narrowing down to a single mode due to the difference in wavelength between the beams, it's a common consequence for any FWM arrangement considering the

phase-matching conditions that arise in the extensive regime.

The following figures illustrate the theoretical results for a combination of modes in the thin and extensive medium regimes, for the cases we were able to measure the FWM signal in the thin regime. Figure 33 shows the results for the combination of gaussian-HG modes, figures 34 and 35 show the results for the combination of HG-HG modes, where $u_A = u_B$ and $u_A \neq u_B$, respectively.

Figure 33 – Theoretical intensity profile for a combination of gaussian-HG modes in the extensive and thin medium regimes. Here, we show the intensity distribution of the incident u_A beam (u_B is gaussian in every case), the distribution of the theoretical nonlinear signal u_{2A-B} for each thickness regime, and diagrams representing the coefficients of the contributing modes to the nonlinear signals.

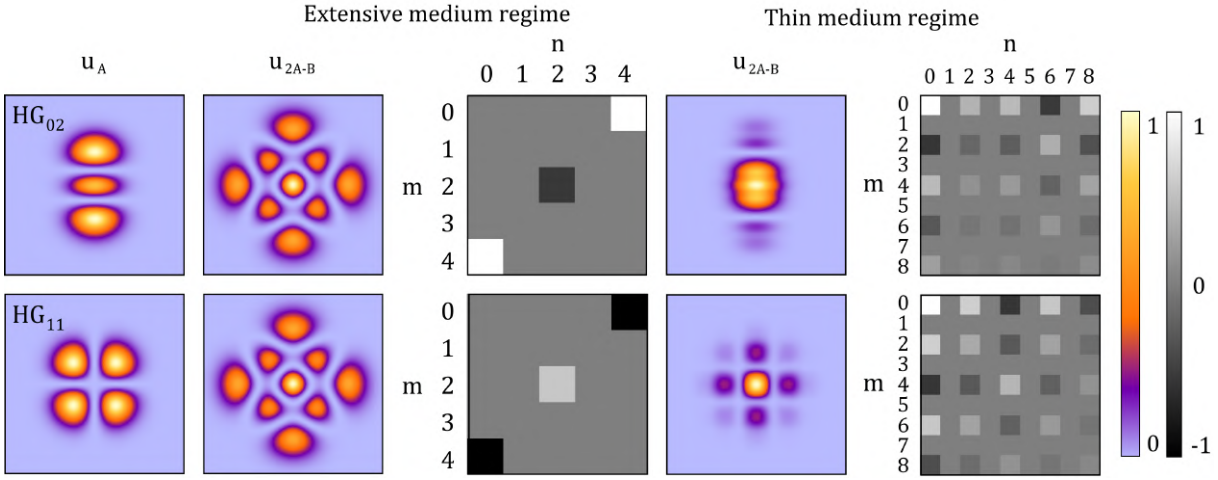

Source: the author (2023).

Figure 34 – Theoretical intensity profile for a combination of HG-HG modes, with $u_A = u_B$, in the extensive and thin medium regimes. Here, we show the intensity distribution of the incident beams, the distribution of the theoretical nonlinear signals for each thickness regime, and diagrams representing the coefficients of the contributing modes to the nonlinear signals.

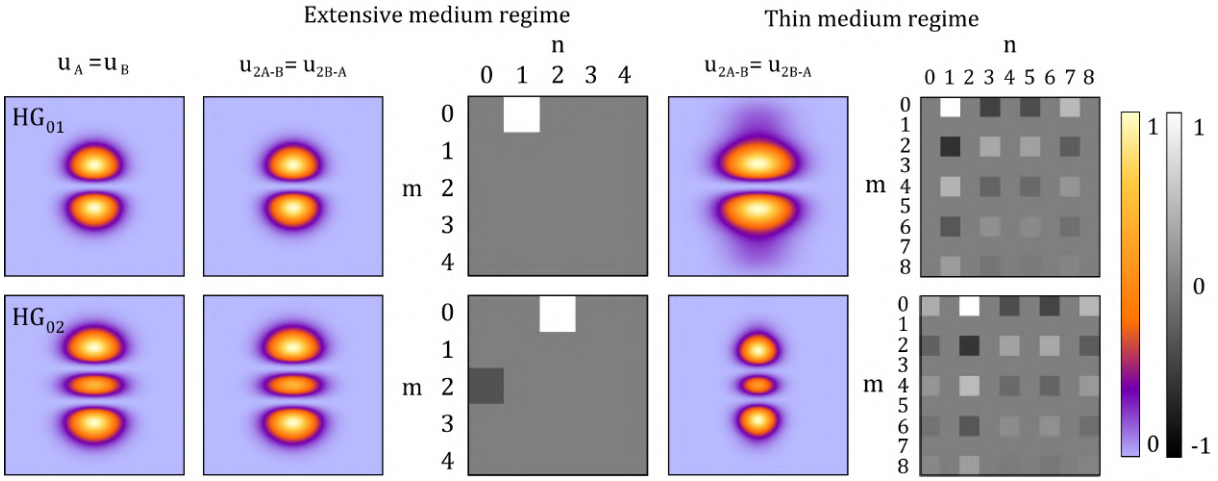

Source: the author (2023).

Figure 35 – Theoretical intensity profile for a combination of HG-HG modes, with $u_A \neq u_B$, in the extensive and thin medium regimes. Here, we show the intensity distribution of the incident beams, the distribution of the theoretical nonlinear signals for each thickness regime, and diagrams representing the coefficients of the contributing modes to the nonlinear signals.

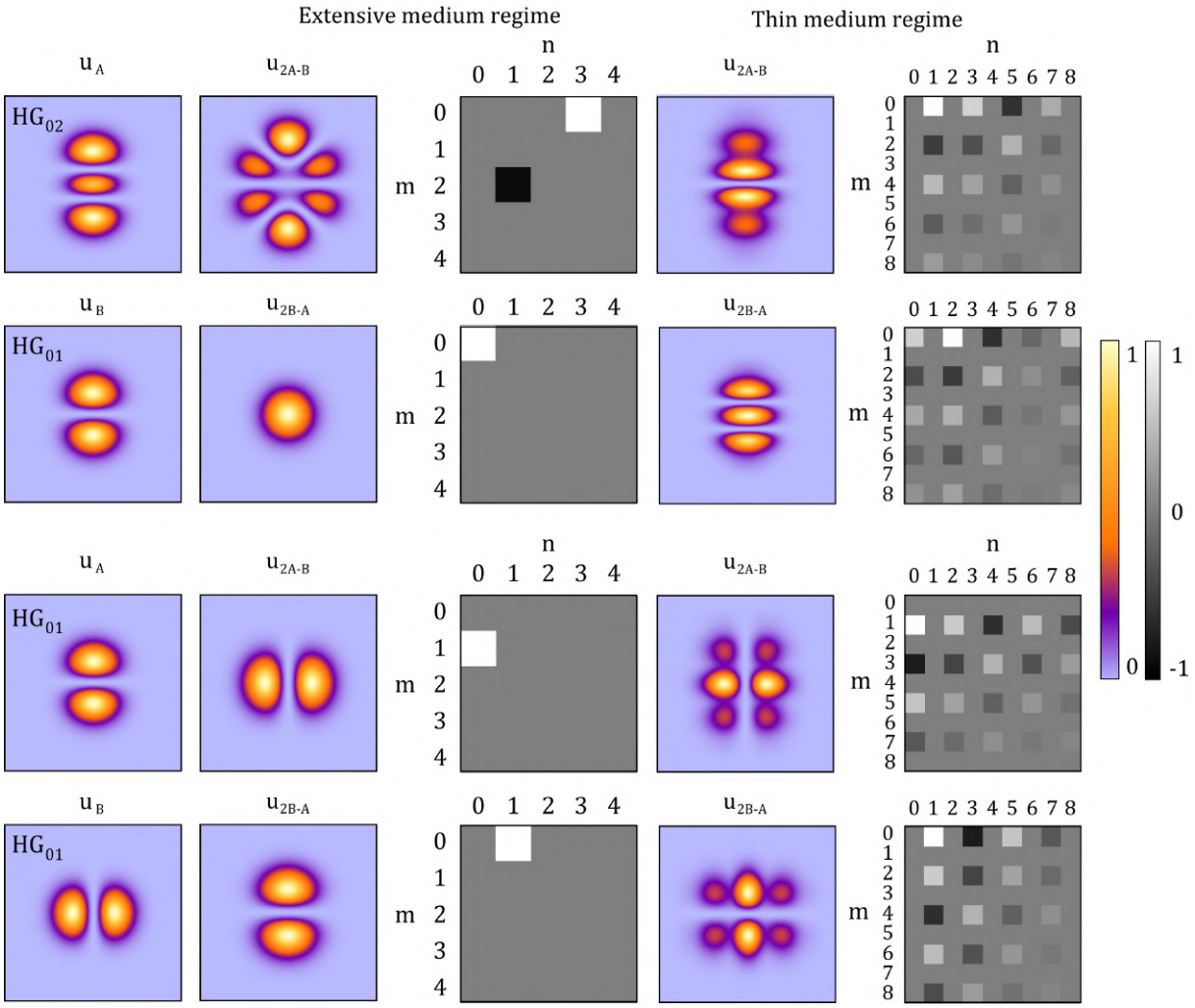

Source: the author (2023).

6 CONCLUSIONS

In this work, we investigated the transfer of transverse modes of Hermite-Gauss beams in a nonlinear optical process, specifically degenerate four-wave mixing in a sample of rubidium vapor. From the theoretical model, we derived selection rules that govern the mode transfer for each thickness regime. In summary, the first selection rule, valid for both regimes, states that the parity of the mode indexes of the generated signals must match the parity of the beam that participates only once in the process. The second selection rule, exclusive to the extensive regime, dictates that the process must conserve mode order, limiting the modes contributing to the generated signals. These selection rules allowed us to obtain the expected intensity profiles of the generated fields and the coefficients of their expansion in terms of the Hermite-Gauss function space.

In the experiment, we successfully obtained results for the thin medium regime. However, we encountered difficulties in the extensive medium regime, primarily due to the small volume of overlap between the incident beams. This significantly reduced the efficiency of the process and made it difficult to detect the generated signal. Furthermore, we encountered challenges regarding the length of overlap between the beams, making it difficult to confidently affirm that we were operating in the extensive medium regime. Additionally, in another instance, we did not meet Boyd's criteria for maximizing efficiency.

Theoretical and experimental results obtained for the thin medium regime showed overall agreement in their shapes, with minor deformations and slight deviations in intensity. The process we studied is known to have low efficiency, and the fact that the generated signals share the same frequency as the incident beams poses difficulties in isolating them from the transmitted beams. The use of spatial filters, such as mechanical blocking of the transmitted beams, leads to the scattering of light, resulting in interference with the generated signals.

In addition, it is interesting to observe distinct results arising only from variations in the sample length, leading to different longitudinal phase matching. By satisfying Boyd's criteria, the phase terms associated with the curvature radius of the beams are eliminated, leaving the longitudinal dependence on the Gouy phase alone.

Further investigation should be directed toward meeting the experimental requirements of the extensive medium regime to obtain measurements for comparison with the theoretical predictions. It is worth noting that these requirements have already been accomplished in a

three-level cascade system [25], where the atomic sample is excited in the infrared, and the nonlinear signal is generated at higher frequencies. This system is more viable as the four-wave mixing can be done with perfectly overlapped incident beams, and the generated signal can be isolated using a spectral filter.

Another perspective involves exploring this system using alternative high-order beam function bases, like Laguerre, Ince, Hypergeometric modes, and more. Furthermore, extending the investigation to include input modes that are not pure in the incident beams A and B. This has only been done in theoretical studies, as seen in [24].

REFERENCES

[1] R. W. Boyd, *Nonlinear optics*, 4th. Academic Press, 2020.

[2] B. Gu, C. Zhao, A. Baev, K.-T. Yong, S. Wen, and P. N. Prasad, "Molecular nonlinear optics: Recent advances and applications", *Advances in Optics and Photonics*, vol. 8, no. 2, p. 328, 2016. DOI: 10.1364/aop.8.000328.

[3] T. Schneider, *Nonlinear Optics in Telecommunications*. Springer, 2004.

[4] R. J. Glauber, "The quantum theory of optical coherence", *Physical Review*, vol. 130, no. 6, pp. 2529–2539, 1963. DOI: 10.1103/physrev.130.2529.

[5] G. N. Lewis, D. Lipkin, and T. T. Magel, "Reversible photochemical processes in rigid media. a study of the phosphorescent state", *Journal of the American Chemical Society*, vol. 63, no. 11, pp. 3005–3018, 1941. DOI: 10.1021/ja01856a043.

[6] T. Maiman, "Stimulated optical radiation in ruby", *Nature*, vol. 187, no. 4736, pp. 493–494, 1960. DOI: 10.1038/187493a0.

[7] P. A. Franken, A. E. Hill, C. W. Peters, and G. Weinreich, "Generation of optical harmonics", *Physical Review Letters*, vol. 7, no. 4, pp. 118–119, 1961. DOI: 10.1103/physrevlett.7.118.

[8] W. Kaiser and C. G. Garrett, "Two-photon excitation in ca", *Physical Review Letters*, vol. 7, no. 6, pp. 229–231, 1961. DOI: 10.1103/physrevlett.7.229.

[9] S. A. Akhmanov, A. I. Kovrigin, A. S. Piskarskas, V. V. Fadeev, and R. V. Khokhlov, "Observation of parametric amplification in the optical range", 1965.

[10] G. D. Boyd and D. A. Kleinman, "Parametric interaction of focused gaussian light beams", *Journal of Applied Physics*, vol. 39, no. 8, pp. 3597–3639, 1968. DOI: 10.1063/1.1656831.

[11] J. A. Armstrong, N. Bloembergen, J. Ducuing, and P. S. Pershan., "Interactions between light waves in a nonlinear dielectric", *Encounters in Nonlinear Optics*, pp. 3–28, 1962. DOI: 10.1142/9789812795793_0001.

[12] P. D. Maker, R. W. Terhune, M. Nisenoff, and C. M. Savage, "Effects of dispersion and focusing on the production of optical harmonics", *Physical Review Letters*, vol. 8, no. 1, pp. 21–22, 1962. DOI: 10.1103/physrevlett.8.21.

[13] R. Pratesi and L. Ronchi, "Generalized gaussian beams in free space", *Journal of the Optical Society of America*, vol. 67, no. 9, p. 1274, 1977. DOI: 10.1364/josa.67.001274.

[14] L. Allen, M. W. Beijersbergen, R. J. Spreeuw, and J. P. Woerdman, "Orbital angular momentum of light and the transformation of laguerre-gaussian laser modes", *Physical Review A*, vol. 45, no. 11, pp. 8185–8189, 1992. DOI: 10.1103/physreva.45.8185.

[15] M. A. Bandres and J. C. Gutiérrez-Vega, "Ince–gaussian beams", *Optics Letters*, vol. 29, no. 2, p. 144, 2004. DOI: 10.1364/ol.29.000144.

[16] H. He, N. Heckenberg, and H. Rubinsztein-Dunlop, "Optical particle trapping with higher-order doughnut beams produced using high efficiency computer generated holograms", *Journal of Modern Optics*, vol. 42, no. 1, pp. 217–223, 1995. DOI: 10.1080/09500349514550171.

[17] G. Gibson *et al.*, "Free-space information transfer using light beams carrying orbital angular momentum", *Optics Express*, vol. 12, no. 22, p. 5448, 2004. DOI: 10.1364/opex.12.005448.

[18] A. Sit *et al.*, "Quantum cryptography with structured photons through a vortex fiber", *Optics Letters*, vol. 43, no. 17, p. 4108, 2018. DOI: 10.1364/ol.43.004108.

[19] M. Granata, C. Buy, R. Ward, and M. Barsuglia, "Higher-order laguerre-gauss mode generation and interferometry for gravitational wave detectors", *Physical Review Letters*, vol. 105, no. 23, 2010. DOI: 10.1103/physrevlett.105.231102.

[20] D. G. Pires, J. C. Rocha, A. J. Jesus-Silva, and E. J. Fonseca, "Optical mode conversion through nonlinear two-wave mixing", *Physical Review A*, vol. 100, no. 4, 2019. DOI: 10.1103/physreva.100.043819.

[21] D. G. Pires, J. C. Rocha, A. J. Jesus-Silva, and E. J. Fonseca, "Higher radial orders of laguerre–gaussian beams in nonlinear wave mixing processes", *Journal of the Optical Society of America B*, vol. 37, no. 5, p. 1328, 2020. DOI: 10.1364/josab.384112.

[22] D. G. Pires, J. C. Rocha, A. J. Jesus-Silva, and E. J. Fonseca, "Interaction of fractional orbital angular momentum in two-wave mixing processes", *Journal of Optics*, vol. 22, no. 3, p. 035 502, 2020. DOI: 10.1088/2040-8986/ab6ae6.

[23] D. G. Pires, J. C. Rocha, M. V. da Silva, A. J. Jesus-Silva, and E. J. Fonseca, "Mixing ince–gaussian modes through sum-frequency generation", *Journal of the Optical Society of America B*, vol. 37, no. 10, p. 2815, 2020. DOI: 10.1364/josab.401001.

[24] J. C. Rocha *et al.*, "Controlled conversion of transverse symmetries in a four-wave mixing process", *Journal of Optics*, vol. 24, no. 4, p. 045 505, 2022. DOI: 10.1088/2040-8986/ac57b2.

[25] R. F. Offer, A. Daffurn, E. Riis, P. F. Griffin, A. S. Arnold, and S. Franke-Arnold, "Gouy phase-matched angular and radial mode conversion in four-wave mixing", *Physical Review A*, vol. 103, no. 2, 2021. DOI: 10.1103/physreva.103.l021502.

[26] A. Yariv, *Quantum Electronics*. John Wiley, 1989.

[27] C. Cohen-Tannoudji, B. Diu, and F. Laloe, "Complement E_{III}: The density operator", in *Quantum Mechanics*, 2nd ed. Wiley, 1977, vol. 1, pp. 295–307.

[28] C. J. Foot, "Section 7.5: Radiative damping", in *Atomic physics*. Oxford University Press, 2005, pp. 134–137.

[29] D. J. Griffiths, "Section 9.3: Electromagnetic waves in matter", in *Introduction to electrodynamics*. Pearson, 2014, pp. 401–411.

[30] E. Hecht, "Chapter 4: The propagation of light", in *Optics*, 4th ed. Addison-Wesley, 2002, pp. 86–137.

[31] M.-K. H. J. W., "Chapter 2: Statistical mechanics of an ideal gas (maxwell)", in *Basics of statistical physics*, 3rd ed. World Scientific, 2022, pp. 11–26.

[32] *Gaussian beam*, Wikimedia Foundation. Available at: https://en.wikipedia.org/wiki/Gaussian_beam, Accessed: June 30, 2023.

[33] E. Hecht, "Chapter 10: Diffraction", in *Optics*, 4th ed. Addison-Wesley, 2002, pp. 443–512.

[34] D. A. Steck, "Rubidium 85 d line data", 2008. pdf: https://steck.us/alkalidata/rubidium85numbers.pdf.

[35] P. A. G. Torres, "Analysis of the transverse spatial image of beams transmitted and generated through a non-linear process in rubidium vapor", MSc. Dissertation, 2022, p. 48.

[36] Z. Zhang, Z. You, and D. Chu, "Fundamentals of phase-only liquid crystal on silicon (lcos) devices", *Light: Science & Applications*, vol. 3, no. 10, 2014. DOI: 10.1038/lsa.2014.94.

[37] *LCOS-SLM X10468/X13267/X13138 series manual*, Hamamatsu Photonics. Available at: https://hamamatsu.su/media/index/?type=catalog&id=115, Accessed: June 9, 2023.

[38] J. Arlt, K. Dholakia, L. Allen, and M. Padgett, "The production of multiringed laguerre–gaussian modes by computer-generated holograms", *Journal of Modern Optics*, vol. 45, no. 6, pp. 1231–1237, 1998. DOI: 10.1080/09500349808230913.

[39] L. G. Neto, D. Roberge, and Y. Sheng, "Full-range, continuous, complex modulation by the use of two coupled-mode liquid-crystal televisions", *Applied Optics*, vol. 35, no. 23, p. 4567, 1996. DOI: 10.1364/ao.35.004567.

[40] R. W. Cohn and M. Liang, "Approximating fully complex spatial modulation with pseudorandom phase-only modulation", *Applied Optics*, vol. 33, no. 20, p. 4406, 1994. DOI: 10.1364/ao.33.004406.

[41] J. A. Davis, D. M. Cottrell, J. Campos, M. J. Yzuel, and I. Moreno, "Encoding amplitude information onto phase-only filters", *Applied Optics*, vol. 38, no. 23, pp. 5004–5013, 1999. DOI: 10.1364/ao.38.005004.

[42] *CCD and CMOS Cameras: DCx Camera Functional Description and SDK Manual*, Thorlabs, Inc. Available at: https://www.thorlabs.com/thorproduct.cfm?partnumber=DCC1545M, Accessed: June 10, 2023.

[43] M. R. L. Motta, "Two symmetric four-wave mixing signals induced by beams with nonuniform distributions", MSc. Dissertation, 2021, pp. 52–55.